# Extracellular Architecture of the SYG-1/SYG-2 Adhesion Complex Instructs Synaptogenesis

Engin Özkan,[1,2] Poh Hui Chia,[3] Ruiqi Rachel Wang,[4] Natalia Goriatcheva,[1,2] Dominika Borek,[5] Zbyszek Otwinowski,[5] Thomas Walz,[4,6] Kang Shen,[2,3] and K. Christopher Garcia[1,2,*]

[1]Department of Molecular and Cellular Physiology and Department of Structural Biology, Stanford University School of Medicine, Stanford, CA 94305, USA
[2]Howard Hughes Medical Institute, Stanford University School of Medicine, Stanford, CA 94305, USA
[3]Department of Biology, Stanford University, Stanford, CA 94305, USA
[4]Department of Cell Biology, Harvard Medical School, Boston, MA 02115, USA
[5]Departments of Biochemistry and Biophysics, University of Texas Southwestern Medical Center at Dallas, Dallas, TX 75390, USA
[6]Howard Hughes Medical Institute, Harvard Medical School, Boston, MA 02115, USA
*Correspondence: kcgarcia@stanford.edu
http://dx.doi.org/10.1016/j.cell.2014.01.004

## SUMMARY

SYG-1 and SYG-2 are multipurpose cell adhesion molecules (CAMs) that have evolved across all major animal taxa to participate in diverse physiological functions, ranging from synapse formation to formation of the kidney filtration barrier. In the crystal structures of several SYG-1 and SYG-2 orthologs and their complexes, we find that SYG-1 orthologs homodimerize through a common, bispecific interface that similarly mediates an unusual orthogonal docking geometry in the heterophilic SYG-1/SYG-2 complex. *C. elegans* SYG-1's specification of proper synapse formation in vivo closely correlates with the heterophilic complex affinity, which appears to be tuned for optimal function. Furthermore, replacement of the interacting domains of SYG-1 and SYG-2 with those from CAM complexes that assume alternative docking geometries or the introduction of segmental flexibility compromised synaptic function. These results suggest that SYG extracellular complexes do not simply act as "molecular velcro" and that their distinct structural features are important in instructing synaptogenesis.

## INTRODUCTION

Cellular adhesion has enabled evolution of multicellular organisms and is a requirement for many different anatomical formations. It is regulated and mediated by interactions between cell surface receptors known as cell adhesion molecules (CAMs), which provide the physical strength of attachment and also define the specificity of cells and subcellular localizations that comprise the adhesive surfaces (Hynes and Zhao, 2000; Yamagata et al., 2003). Furthermore, these receptors can signal to

initiate processes that lead to functional differentiation into one of many specific cellular adhesion structures, such as neuronal and immune synapses. However, the role of extracellular structure and ligand-receptor affinity in modulating the plethora of functions resulting from CAM engagement is not well understood. It is not clear whether adhesion is structurally permissive and simply serves as "molecular velcro" or whether the biophysical characteristics of the interactions are critical in triggering distinct functional outcomes.

A group of CAMs utilized in animals in many different adhesion structures is the family of proteins homologous to *C. elegans* SYG-1 and SYG-2, which are immunoglobulin superfamily (IgSF) CAMs (Ig-CAMs) (Figure 1A) (Shen and Bargmann, 2003; Shen et al., 2004). These proteins not only specify synaptogenesis by mediating adhesion between guidepost vulval epithelial cells and the axon of the hermaphrodite-specific neurons (HSN) in *C. elegans* (Figure 1A), but also have adopted many other functions in arthropods and in vertebrates. SYG-1 and SYG-2 homologs are known to mediate muscle formation by specifying the fusion of muscle progenitor cells (myoblasts) in *Drosophila* and vertebrates (Dworak et al., 2001; Sohn et al., 2009; reviewed in Abmayr and Pavlath, 2012). They also control other processes in *Drosophila* that involve formation of proper cellular adhesions, such as the precise patterning of cells in the eye (Bao and Cagan, 2005; Ramos et al., 1993; Wolff and Ready, 1991) and sense organ spacing on the antennae (Venugopala Reddy et al., 1999), and are crucial in accurate formation of the optic chiasm (Boschert et al., 1990; Ramos et al., 1993; Schneider et al., 1995). Vertebrate orthologs of both proteins are strongly expressed in the nervous system, where new functions for the orthologous Neph proteins are emerging (Mizuhara et al., 2010; Serizawa et al., 2006; Völker et al., 2012). Intriguingly, orthologs of SYG-1 and SYG-2 have also been adopted in arthropods and vertebrates for building the hemolymph and blood filtration barriers, respectively, confirming that the two organs are evolutionarily related (Weavers et al., 2009). Mutations in the human SYG-2 ortholog, Nephrin, lead to a kidney
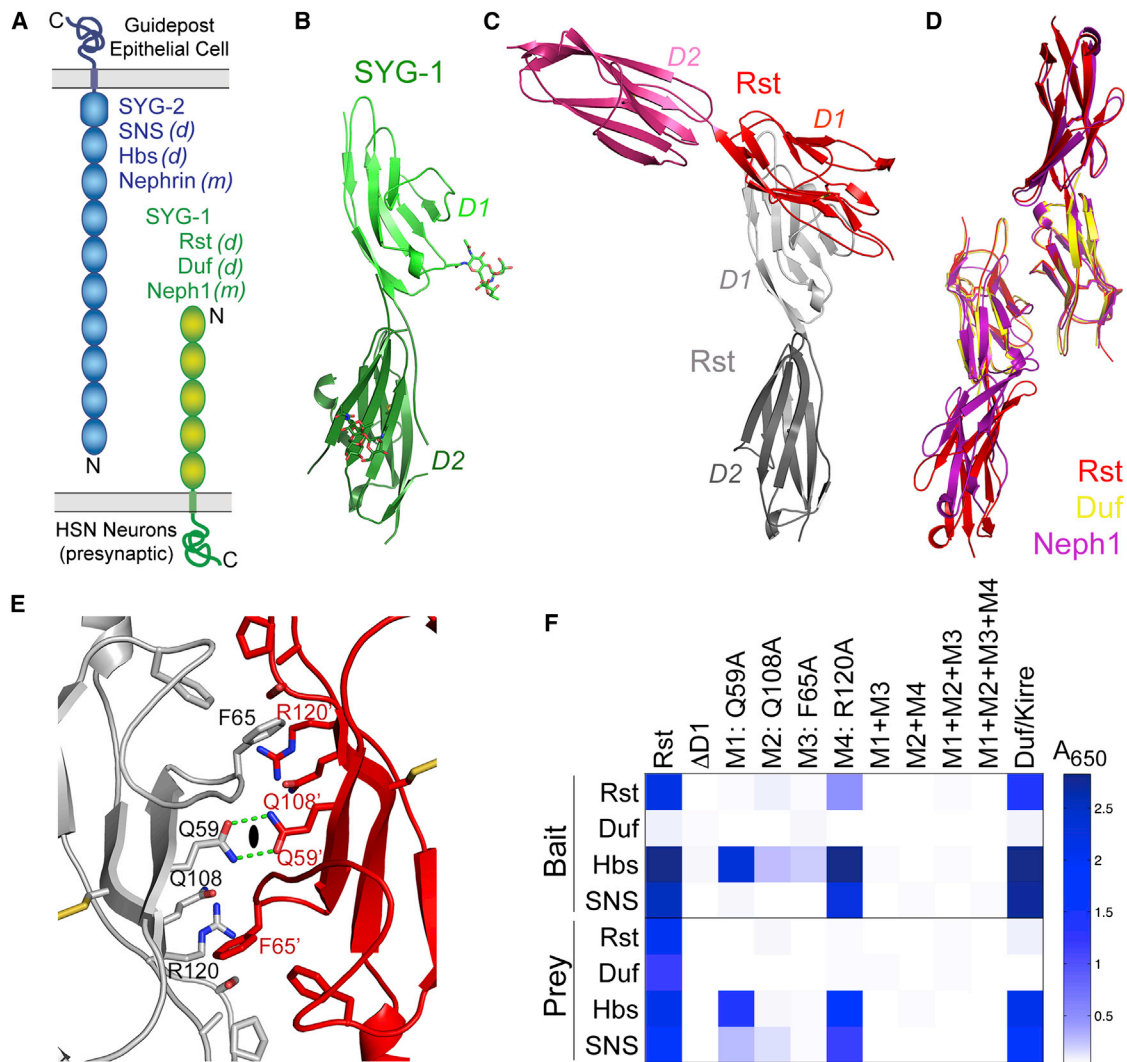
**Figure 1. Structures of SYG-1 and Homodimeric SYG-1-like Complexes**

(A) Schematic representation of the domain structures of SYG-1 and SYG-2. All domains are of the Ig type except for the last domain of SYG-2, which is from the related FnIII domain family. Also noted are the *Drosophila melanogaster* (*d*) and mammalian (*m*) orthologs.

(B) The crystal structure of *C. elegans* SYG-1 domains 1 and 2 (D1 and D2) in light and dark green, respectively. N-linked glycosylation is depicted in sticks representation.

(C) The homodimeric structure of Rst D1-D2, demonstrating the near-orthogonal approach of the monomers.

(D) Overlay of structures solved of *Drosophila* and mouse SYG-1-like proteins. The close match between the homodimeric structures of Rst (red and orange), Duf/Kirre (yellow), and Neph1 (purple) demonstrate that the crystallographically observed homodimers are conserved and physiological.

(E) Close-up of the symmetrical Rst homodimer interface. The 2-fold sign (closed oval) represents the homodimer symmetry axis. The prime sign is added to residue labels for the Rst monomer displayed in red.

(F) The extracellular interactome assay (Özkan et al., 2013) for wild-type Rst and mutants against wild-type Rst, Duf, Hbs, and SNS. The assay was performed in both orientations, as wild-type Rst, Duf, Hbs, and SNS as bait (above) and as prey (below). The scale, colored as white to blue, represents absorbance values at 650 nm as the assay outcome.

See also Figure S1 and Table S1.

disease called the congenital nephrotic syndrome of the Finnish type (Kestilä et al., 1998). SYG family proteins, therefore, constitute one of the most important and versatile CAMs in metazoans, involved in disparate cell adhesion functions ranging from synaptogenesis to blood filtration in kidney. Despite their prominence, the membrane-proximal downstream signaling events that result from extracellular engagement of SYGs and their

orthologs are not entirely clear. Vertebrate Nephrins are known to be phosphorylated, which leads to actin attachment (Jones et al., 2006; Verma et al., 2006), whereas F-actin is recruited for SYG-specified synapse development in *C. elegans* (Chia et al., 2012). *C. elegans* SYG-1 also controls synapse elimination through directly inhibiting the ubiquitin ligase SCF[SEL-10] (Ding et al., 2007). The most conserved intracellular feature of SYGs,

a C-terminal PDZ domain-binding peptide, mediates interactions with juxtamembrane scaffolding proteins such as ZO-1 and X11Lα (Huber et al., 2003; Vishnu et al., 2006).

Despite their importance in many aspects of animal physiology, the molecular basis of SYG-1 and SYG-2 interactions at cellular adhesion sites and the role of structure in specifying function are not known. Here, we ask whether the structural and biophysical features of SYG extracellular complexes are important for conveying a proper functional outcome. Through a series of biochemical, biophysical, and in vivo functional experiments, we find that the extracellular affinity, docking geometry, and rigidity of the SYG-1 and SYG-2 ectodomains play crucial roles in specifying a functional synaptic architecture in *C. elegans*.

## RESULTS

### Interactions of SYG-1/SYG-2 Complexes

The relative abilities of SYGs and their orthologs to form homo-versus heterophilic complexes reflect the acquisition of functional specification and response to evolutionary pressures unique to each phylum. However, it is not clear which SYGs engage one another directly. Thus, we measured the homo- and heterotypic interactions between a variety of SYG-1- and SYG-2-related proteins (Figure 1A), which were previously studied with cell aggregation assays and by coimmunoprecipitation and had yielded conflicting conclusions (Bao and Cagan, 2005; Dworak et al., 2001; Galletta et al., 2004; Gerke et al., 2003; Khoshnoodi et al., 2003; Schneider et al., 1995; Shelton et al., 2009; Wanner et al., 2011). Using isothermal titration calorimetry (ITC) and surface plasmon resonance (SPR), we showed that *C. elegans* SYG-1 and SYG-2 ectodomains form a complex with a dissociation constant ($K_d$) of ∼0.6 μM (Figure S1 and Table S1 available online). We also expressed the first immunoglobulin (Ig) domain of SYG-1 and the first four Ig domains of SYG-2 for crystallization, and these bound with similar affinity as the full-length ectodomains (Figure S1 and Table S1).

These interactions are conserved across SYG orthologs, as we showed that the *Drosophila* homologs of SYG-1 (Rst and Duf/Kirre) and of SYG-2 (SNS and Hbs) all form heterocomplexes with affinities between 1 and 4 μM (Figure S2 and Table S1). Minimal complex-forming regions of the homologous *Drosophila* system were similarly mapped to within the first Ig domain of Rst or Duf and the first four Ig domains of SNS or Hbs (Figure S2 and Table S1). The similarity of the ectodomain interaction parameters among *Drosophila* and *C. elegans* SYGs suggests that this moderate affinity has been evolutionarily refined as optimal for SYG function.

Various SYG-1- and SYG-2-like proteins have been previously reported to form homophilic complexes (Dworak et al., 2001; Gerke et al., 2003; Khoshnoodi et al., 2003; Schneider et al., 1995; Wanner et al., 2011); we did not detect high-affinity homophilic complexes for SYG-1, SYG-2, and their *Drosophila* orthologs. However, using a multivalent assay format to enhance avidity that we recently developed for detecting extracellular interactions (Özkan et al., 2013), we observed the reported Rst and Neph1 homophilic complexes (Gerke et al., 2003; Liu et al., 2003; Schneider et al., 1995) and a complex of Rst and Duf (Özkan et al., 2013), all of which are SYG-1-like proteins. We showed with SPR that the Rst homophilic complex was very low affinity (Figure S2I). We did not detect a *C. elegans* SYG-1 homophilic complex or homophilic and heterophilic complexes between any SYG-2, which is in agreement with the previous reports on SYG interactions using S2 cell aggregation assays for *C. elegans* and *Drosophila* SYGs (Shen et al., 2004; Dworak et al., 2001). We cannot, however, rule out very weak *cis*-homophilic interactions for SYG-1 and SYG-2, as suggested by Shelton et al. (2009) and Wanner et al. (2011).

### Structure of SYG-1: A Conserved Homodimeric Interface

To acquire molecular insights into SYG-1 surfaces and the homophilic interactions of its orthologs, we first determined the crystal structures of the first domain (D1) and the first two domains (D1D2) of *C. elegans* SYG-1 (Figure 1B and Table S2). The D1 and D2 domains both adopt the canonical immunoglobulin fold with two β sheets and a conserved disulfide bond linking the sheets through the B and F strands (Bork et al., 1994). The Ig domains are colinear, exhibiting extensive interdomain contacts and segmental rigidity due to the absence of linker residues between the two domains (Figure S4A). We did not observe homodimers for any of these structures.

We then determined crystal structures of D1D2 of *Drosophila* Rst, the D1 of *Drosophila* Duf, and the D1D2 of mouse Neph1. In contrast to *C. elegans* SYG-1, we observe homodimeric structures for all of these SYG-1 orthologs mediated entirely by their D1 domains, which is consistent with our biochemical data (Figure 1C, Rst is shown). The homodimers are formed through interactions between the C′CFG sheets of the Ig domains (Figures 1C and 1D). The monomers create homodimers by docking against each other at nearly orthogonal angles of 90° to 110° (Figure 1C), and this interaction geometry is conserved between the three SYG-1-like homodimers. The buried surface area of the homodimers is 1,270 Å² ± 50 Å². These structures argue that arthropod and mammalian, but not nematode, SYG-1 orthologs homodimerize via the observed common interface.

Three residues are prominent within the homophilic interface: Q59, F65, and Q108 in Rst sequence numbering (Figure 1E). The 2-fold symmetry axis relating the complex monomers bisects the two Q59 residues, whose contacts are mediated by two hydrogen bonds. F65 sits in a pocket, packing against the side chain of Q108. To probe the energetic landscape of this interface, we used the extracellular interactome assay (Özkan et al., 2013) to detect Rst homodimerization (Figures 1E and 1F). We mutated Q59, F65, Q108, and R120, another F65-contacting residue. Alanine mutations of Q59 and F65 abolished the interaction, whereas Q108 and R120 diminished it significantly (Figure 1F). Q59 and Q108 are conserved in all SYG-1s, R120 is conserved in all nonnematode SYG-1s, and F65 is part of a conserved hydrophobic patch (Figure 3D). Interestingly, all the mutations measured in the interactome assay that diminished homophilic interactions also diminished the heterophilic interactions (Figure 1F), indicating that these interaction interfaces overlap.
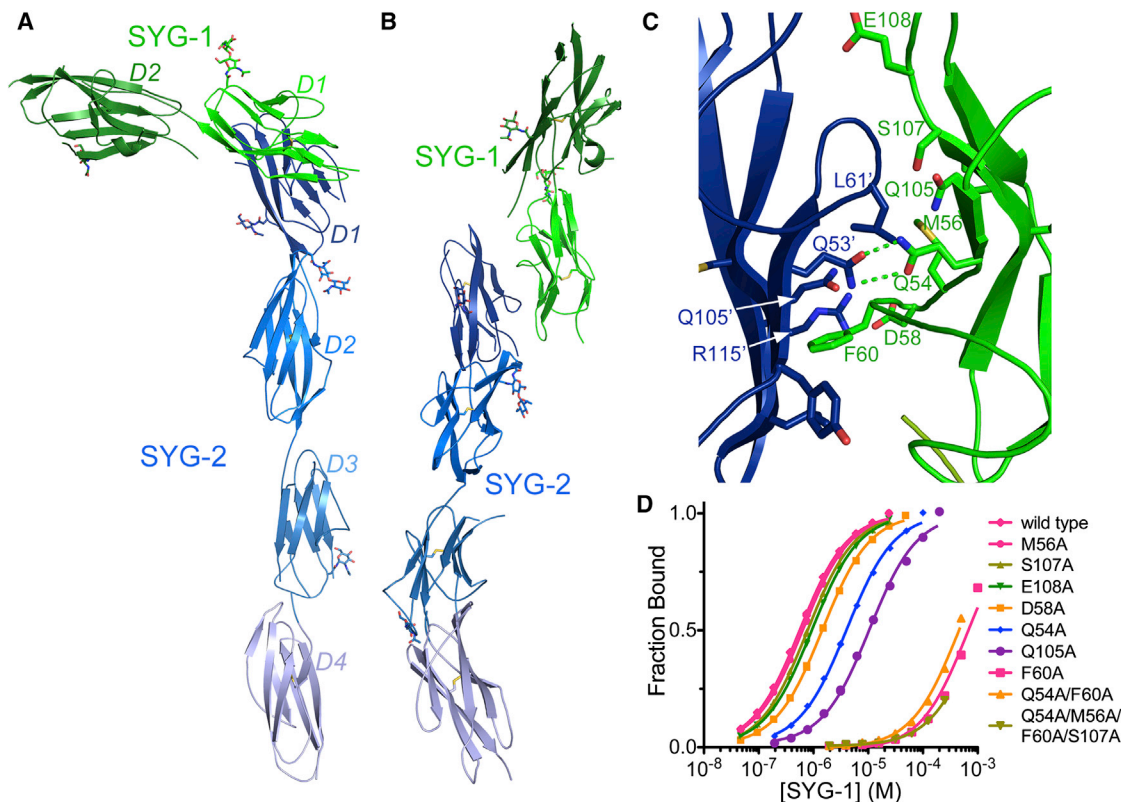
**Figure 2. Structure of the SYG-1/SYG-2 Heterophilic Complex**

(A and B) Two different views of the crystal structure of the complex of SYG-1 (green) and SYG-2 (blue) in which individual Ig domains are labeled in different shades of the respective colors. N-linked glycosylation is represented as sticks. See Table S2 for crystallography statistics.

(C) Close-up view of the SYG-1/SYG-2 heterophilic interface. Prime signed residue labels belong to SYG-2 residues.

(D) Binding isotherms for the interactions of wild-type and mutant SYG-1 with SYG-2 as measured by SPR. See Figure S2 for SPR data for *Drosophila* SYGs.

## Structure of the SYG-1/SYG-2 Heterophilic Complex

To visualize the molecular basis of the heterophilic interaction, we determined the crystal structure of the *C. elegans* SYG-1/SYG-2 complex containing the two N-terminal Ig domains of SYG-1 and the four N-terminal Ig domains of SYG-2 (Figures 2A and 2B). We solved the structure in several steps, using molecular replacement with our two-domain SYG-1 structure, de novo phasing of the fourth domain of SYG-2, followed by manual building of the remaining SYG-2 domains aided by a SYG-2 D3D4 crystal structure.

In accord with prior structure-function analysis (Chao and Shen, 2008) and in vitro mutational binding results (Figure 1F), the interaction between SYG-1 and SYG-2 is mediated entirely by their N-terminal Ig domains (D1). The D1s of SYG-1 and SYG-2 engage each other orthogonally at an ∼108° angle, resulting in an unusual L-like shape for the overall complex structure (Figures 2A and 2B). All the domains are colinear with each molecule in an extended conformation due to the lack of linker residues between the domains, resulting in extensive interdomain contacts (Figures S4A–S4C) and an overall rigidification of the molecules (Figure 2).

We interrogated the heterophilic interface by measuring the effects of mutations on SYG-1–SYG-2 binding affinity using SPR (Figures 2C and 2D and S3). SYG-1 residues central to the heterophilic interface and crucial for the interaction affinity are F60, Q105, and Q54, which are the equivalent residues that abolished the Rst homophilic interaction when mutated (Figure 1F). At the center of the interface, SYG-1 Q54 interacts with SYG-2 Q53 in the same manner as seen for the Rst Q59 in the homodimer. SYG-1 F60 packs against SYG-2 Q105 within a pocket lined by SYG-2's F strand; these two residues are equivalent to Rst F65 and Q108, respectively. For SYG-2, the residue homologous to Rst F65 and SYG-1 F60 is a leucine (L61), which forms part of the C-C′ loop of the Ig domain. This loop makes close van der Waals contacts to SYG-1 Q105. We also mutated the SYG-2 residues related to SYG-1/Rst residues Q54/Q59, F60/F65, Q105/Q108, and V116/R120; namely Q53, L61, Q105 and R115 (Figure S3B). Alanine mutagenesis of Q53, L61, and R115 caused an 80- to 330-fold loss in affinity, and Ala mutation of Q105, which packs against the crucial F60 of SYG-1, essentially abolished the interaction. Thus, the energetic parsing of the interface reveals an asymmetry, whereby the SYG-1-F60-SYG-2-Q105 pair is more energetically important for binding than its structurally symmetric SYG-2-L61-SYG-1-Q105 pair.
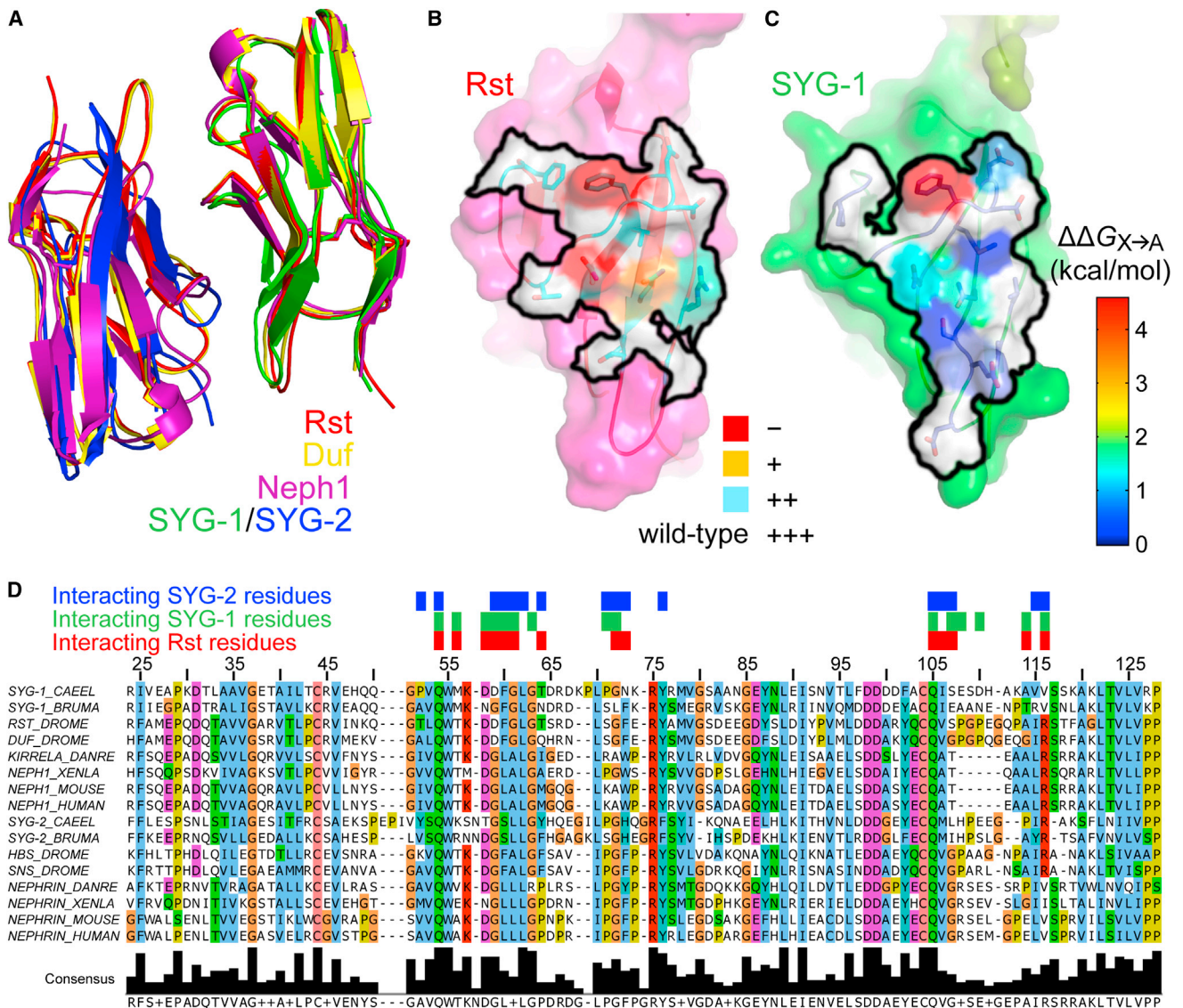
**Figure 3. Comparison of Homophilic and Heterophilic SYG-like Complexes**

(A) D1s in four complex structures are overlaid to demonstrate the conservation between the homophilic and heterophilic binding modes.

(B) Surface representation of the interaction footprint (black outline) in the homodimeric Rst complex. The outline includes residues within 4 Å of the other Rst monomer. Cyan, orange, and red represent increasing loss of binding as observed in Figure 1F upon mutagenesis of the labeled residues to alanine.

(C) Surface representation of the interaction footprint (black outline) of the SYG-1/SYG-2 complex on SYG-1. Within the black outline, blue to red coloring indicates increased loss of binding upon mutagenesis—as measured in Figure 2D—but converted to change in free energy.

(D) Sequence alignment of the first domains (D1) of SYG-1-like and SYG-2-like proteins from the nematodes *C. elegans* and *Brugia malayi*, fruit fly (*D. melanogaster*), zebrafish (*D. rerio*), frog (*X. laevis*), mouse, and human. The sequence numbering is for the *C. elegans* SYG-1. The red, green, and blue boxes above the sequences represent residues of Rst, *C. elegans* SYG-1, and *C. elegans* SYG-2 that are within 4 Å of their interaction partners. See also Figure S3.

## The Homophilic and Heterophilic Complexes of SYG-like Proteins Are Mediated by Bispecific Interfaces and Common Docking Geometries

The amino acid contacts mediating the heterophilic SYG-1/SYG-2 complex closely mimic those mediating the homophilic complex interface, revealing a highly uncommon dual specificity within one binding site. First, the heterocomplex of the SYG-1 and SYG-2 D1 domains is essentially superimposable with homodimeric complexes of Rst, Neph1, and Duf with an average of 1.1 ± 0.2 Å root-mean-square deviation (Figure 3A). Second, the SYG-1 residues participating in the homo- and heterophilic interfaces are nearly identical, all belonging to the C'CFG faces of the Ig domains (Figures 3B–3D). Third, loss of both homo- and heterophilic binding is observed when related residues in *C. elegans* SYG-1 and *Drosophila* Rst are mutated (Figures 1F, 3B, and 3C). The interaction footprints of the homophilic binding
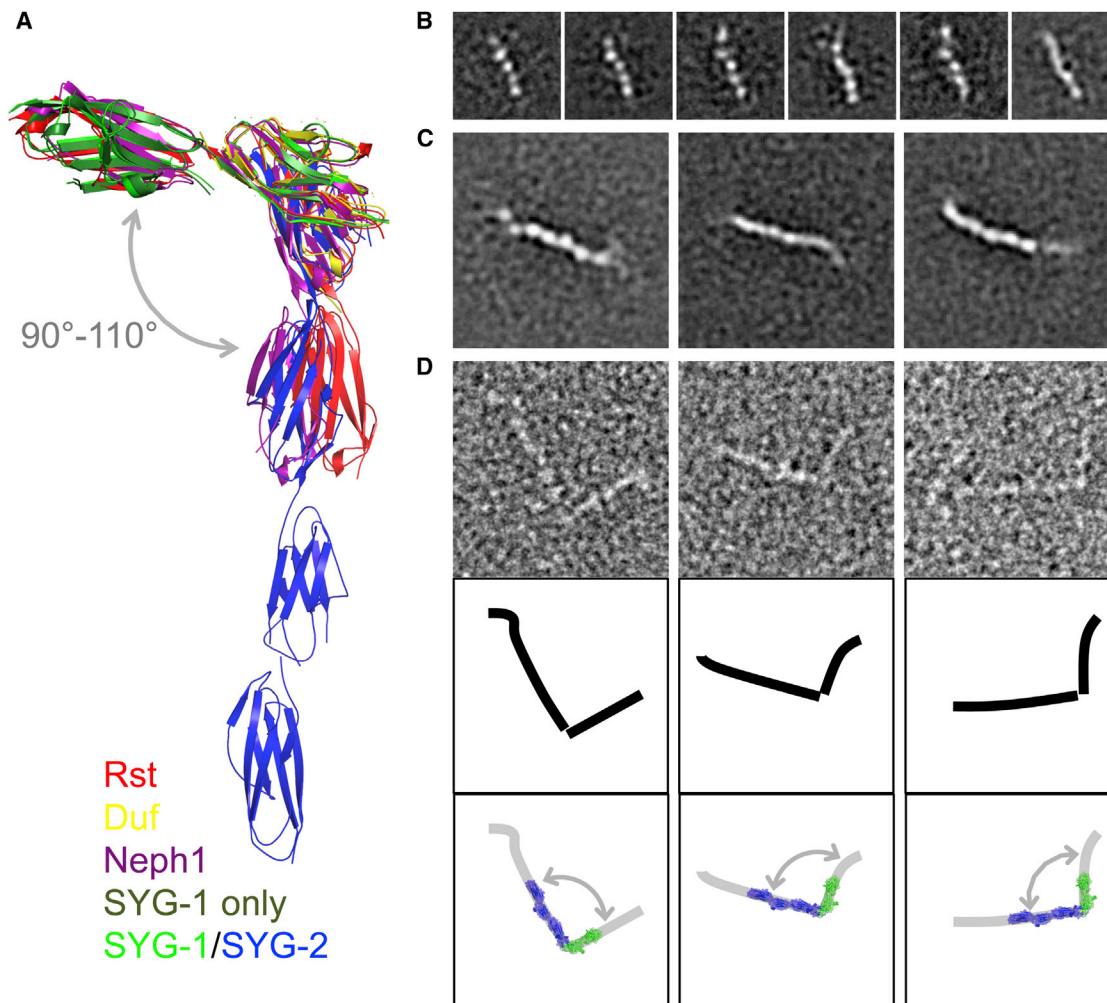
**Figure 4. SYG-1 and SYG-2 Exist in Extended Conformations**

(A) Overlay of five SYG-1 and SYG-1/SYG-2-like complexes solved. The overlay demonstrates that there are only minor movements ("swings") between the domains.

(B–D) Electron microscopy of negatively stained SYG-1 and SYG-2. The side length of the individual panels is 25 nm in (B) and 50 nm in (C) and (D).

(B) Selected class averages of the five domain ectodomain of Syg-1. All class averages are shown in Figure S4A.

(C) Selected class averages of the ectodomain of SYG-2. All class averages are shown in Figure S4B.

(D) Raw particle images of SYG-1/SYG-2 complexes (top), schematic drawings (middle), and the schematic drawings overlaid with the crystal structure of SYG-1-D1-D2/SYG-2-D1-D4 (bottom).

See also Figures S4C–S4G.

partner on Rst (Figure 3B) and the heterophilic binding partner on SYG-1 (Figure 3C) show similar surfaces and energetic contributions to their respective interactions, with the phenylalanine (F60) and the two glutamines (Q54 and Q105 in SYG-1) being most prominent. The patterns of conservation between SYG-1- and SYG-2-like proteins are a result of the "pseudo"-symmetric nature of the heterophilic interactions, which also allows for the symmetric homophilic interaction.

## Full Ectodomain Structures of SYG-1 and SYG-2 and Their Complex

Despite being extended structures with multiple interdomain "joints," the similarity in the individual Ig domain positions of the SYGs and their orthologs is remarkable (Figure 4A). This highlights a surprising rigidity that contrasts with the notion of "beads on a string" for multidomain CAM proteins with flexible domain boundaries. The rigidity of the SYGs is due to the lack of linker sequences between the Ig domains, forcing close-packed domain boundaries that restrain flexibility (Figures S4A–S4C). This inflexibility could perhaps contribute to formation of a relatively rigid mesh comprised of clustered SYG-1 and SYG-2 molecules at the site of a cell adhesion, such as the kidney filtration barrier. Rigidity would also more sensitively convey extracellular engagement to intracellular adaptor proteins. To gain a better appreciation of this issue, we studied the full-length free SYG-1 and SYG-2 ectodomains and the

ectodomain heterodimer by negative-stain electron microscopy (EM) (Figures 4B–4D). The molecules exhibited some regions of flexibility, potentially through small interdomain movements, resulting in parts of some of the molecules missing from most class averages, especially in the ten domain SYG-2 (Figures S4D–S4F). Even small deviations in position would result in exclusion of these regions from averaged images. However, some averages showed the entire five domain SYG-1 ectodomain (Figure 4B) and up to eight domains of the SYG-2 ectodomain (Figure 4C). Averages mostly show extended conformations; we do not see "bent" molecules (Figures S4D–S4F). We also observe 1:1 SYG-1/SYG-2 complexes with an orthogonal topology of interaction that is identical to that seen in the crystal structures (Figures 4D, S4F, and S4G). Therefore, the EM images of the complex are consistent with extended structures lacking major interdomain flexibility and the orthogonal approach observed in our crystal structures.

## SYG-1/SYG-2 Affinity Correlates with Its Synapse Specification Function In Vivo

The SYG-1/SYG-2 complex structure can serve as a guide for testing the functional consequences of disrupting this interaction in vivo. The interaction of SYG-1 with SYG-2 has been implicated in instructing the HSN neurons to form synapses specifically at the vulva region (Shen and Bargmann, 2003; Shen et al., 2004). HSN forms en passant synapses onto vulval muscles that are clustered in a short and stereotyped segment (about 10 μm) of the HSN axon (Figures 5A and 5C). In syg-1 mutants, synaptic material fail to accumulate in the normal synaptic region and form ectopic synaptic clusters in the anterior axon (Figures 5B and 5D). If the SYG-1-SYG-2 interaction is controlling this event, we hypothesized that the interface we observed could be mutated to affect synaptogenesis at the vulva. We injected syg-1 mutant animals with wild-type and SYG-2-binding mutants of syg-1 under the control of the unc-86 promoter, known to drive expression in the HSN neurons (Shen and Bargmann, 2003) (Figures 5E–5H). As shown previously, we observed that wild-type SYG-1 completely rescued the synaptic vesicle clustering defects of syg-1 mutants (Figure 5E), which we could measure either using quantitative fluorescence measurements of synaptic clusters on anterior sites on HSNL or by a manual scoring of this phenotype in multiple independent transgenic lines (n ≥ 50 animals for each line). The SYG-1 mutants selected covered a wide range of SYG-2 affinities, from 1.6-fold to 1,000-fold weaker than wild-type. Mutant SYG-1 with mildly diminished affinity, such as D58A, only partially rescued the wild-type phenotype (Figure 5F), whereas mutations that practically abolished the interaction, such as F60A and the quadruple mutant, resulted in very little rescue of defects in syg-1 mutants (Figures 5G and 5H). As expected, SYG-1 localization at HSN synapses is also dependent on SYG-1's affinity for SYG-2 (Figure S5). Overall, we observe a strong correlation between engineered affinities of the SYG-1-SYG-2 interaction with the rescue of the syg-1 mutant defects (Figure 5I). Importantly, we find that even minor reductions in affinity (i.e., 1.6-fold) cause a synaptogenic defect, speaking to an endogenous interaction strength that is finely poised at a functional threshold. This suggests that the SYG-1/SYG-2 interface we have observed is the upstream controller of synaptogenesis of HSN neurons at the vulva and that the strength of the SYG-1-SYG-2 interaction is an important determinant for the efficiency of synaptogenesis.

## SYG-1/SYG-2 Interaction Modules Can Be Replaced with Orthologous Parts from Drosophila and Mouse Proteins In Vivo

Based on the similarities between the heterophilic complex of C. elegans SYG-1/SYG-2 and the homophilic complexes of arthropod and mammalian homologs, other heterocomplexes likely share the same structural features, including engagement geometry and interacting residues. Two studies have demonstrated that the full-length mouse SYG-1 and SYG-2 orthologs can partially rescue the synaptogenesis defects of syg-1 and syg-2 mutant worms (Neumann-Haefelin et al., 2010; Wanner et al., 2011). With new structural insight to guide us, we tested whether D1 domains from the arthropod (Rst and SNS) and mammalian SYGs (Neph1 and Nephrin) can replace the D1s of SYG-1 and SYG-2 to rescue synapse defects in worms (Figure 6). For this purpose, we used syg-1;syg-2 double-mutant animals and coinjected them with chimeric syg-1 and chimeric syg-2 under the unc-86 and egl-17 promoters, respectively. The egl-17 promoter drives expression in the secondary vulva epithelial cells, and expression of syg-2 with this promoter has been shown to reconstitute synapses in an axonal fragment contacting these cells (Figures 6A–6D) (Shen et al., 2004). We observed that chimeras with Drosophila and mouse D1s can rescue the syg-1;syg-2 phenotype (Figures 6E and 6F). However, the chimeric rescue was observed to be not as efficient as it was with wild-type. We observed rescue in 79% of animals with syg-1/syg-2 coinjections but only in 38% and 23% of arthropod and mammalian chimeras, respectively (tabulated in Figure S6A). The partial penetrance is likely due to lower affinity on the part of the chimeras, which is 5-fold weaker for Rst and SNS (Figures S1, S2, and 7B). Similarly, SYG-1 Q54 mutant with an affinity 7-fold weaker than wild-type SYG-1 rescued syg-1 in only 59% of animals, compared to 96% for wild-type (Figure 5I, by phenotype penetrance). Nevertheless, the rescues are statistically very significant (p < 0.001) compared to the controls of syg-1-only and syg-2-only injections (Figure S6A) and provide further evidence that SYG-1–SYG-2 molecular interactions are evolutionarily conserved across diverse taxa within metazoans.

Wanner et al. (2011) had observed that C. elegans SYG-1 could interact homophilically. We expressed syg-1 with the egl-17 promoter in a syg-2 mutant background in an attempt to replace the SYG-1/SYG-2 complex with SYG-1 homodimers. We did not observe any rescue of the syg-2 mutant phenotype (Figures S6C and S6D), which strengthens our view that nematode SYG-1 does not homodimerize, especially in a transcellular mode.

## The Observed Docking Geometry and Rigidity of SYG-1 and SYG-2 Are Necessary for SYG-1/SYG-2 Complex Function In Vivo

We probed whether the orthogonal docking geometry seen in the SYG-1 and SYG-2 complexes is a necessary feature for synaptogenesis in vivo. For this, we inspected published structures of alternative heterophilic Ig-CAM complexes. When one
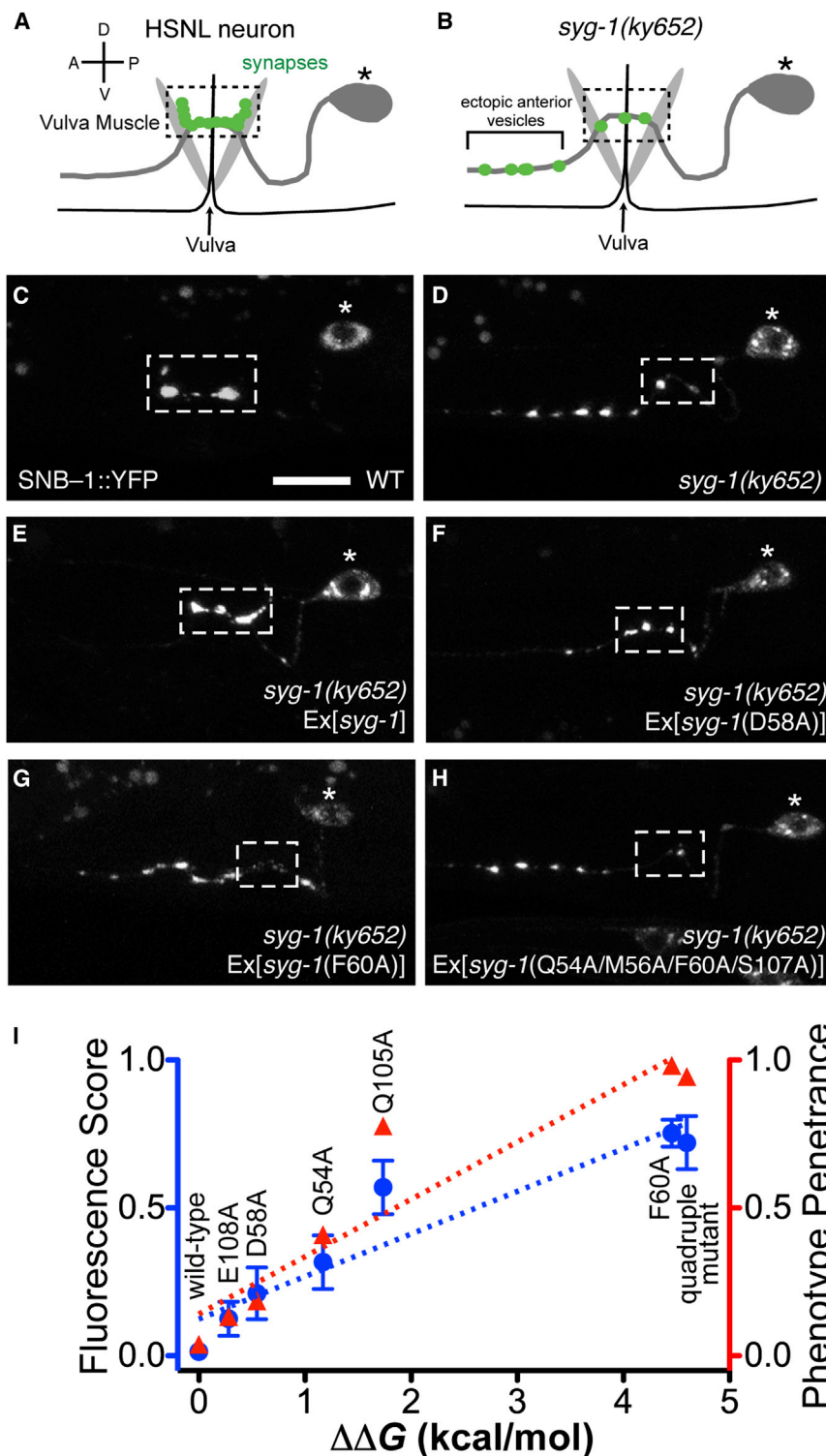
**Figure 5. Affinity of the SYG-1/SYG-2 Complex Correlates with Synaptic Vesicle Defects at the HSNL Neuron**

(A and B) Schematic representation of HSNL synapses at the vulva in wild-type (A) and syg-1 worms (B). The dashed box shows wild-type synaptic region.

(C) Wild-type worms make synapses only at the primary synaptic region at the vulva (within the box).

(D and E) syg-1 animals show ectopic anterior synaptic vesicles. This is rescued when wild-type syg-1 is expressed in HSN.

(F) SYG-1 D58A, a mutant with moderate loss of SYG-1 affinity, partially rescues the syg-1 mutant synaptic vesicle phenotype.

(G and H) SYG-1 F60A and the quadruple mutant, neither of which have appreciable affinity for SYG-2, do not rescue the syg-1 phenotype.

(I) Correlation between affinities of SYG-1 mutants and the syg-1 phenotype. The syg-1 synaptic vesicle phenotype has been measured as both a fluorescence score, a quantitation of ectopic anterior vesicles over ~10 animals, and as a phenotype penetrance score, an all (1), partial (0.5), or none (0) scoring of the synaptic vesicle phenotype in >100 animals. These are compared against loss of binding energy upon the indicated mutations in SYG-1 and show very high correlations to the fluorescence score ($R^2$ = 0.89, blue dashed line) and to the phenotype penetrance ($R^2$ = 0.88, red dashed line). See Figure S5 for SYG-1 clustering at the vulva.

like (JAML) protein with the mouse coxsackie and adenovirus receptor (CAR) has the most similar interaction geometry to the SYG-1/SYG-2 complex (Verdino et al., 2010), with an 8 Å center-of-mass translation of CAR in relation to SYG-2, whereas the Sirpα/CD47 complex is the most structurally divergent (Hatherley et al., 2008), with CD47 displaced ~23 Å from the corresponding position of SYG-2 (Figure 7A). Both complexes have affinities within an order of magnitude of the affinity for the SYG-1/SYG-2 complex, and therefore we reasoned that their D1 domains might functionally substitute for the SYG-1 or SYG-2 D1 domains (Figure 7B) (Hatherley et al., 2008; Verdino et al., 2010).

We coinjected syg-1;syg-2 animals with the mCAR-syg-1 and mJAML-syg-2 and also CD47-syg-1 and Sirpα-syg-2 chimeras. We find that CAR and JAML

of the domains of the alternative complexes is aligned with SYG-1 D1, as in Figure 7A, the orientations of the interaction partners display the spectrum of docking geometries Ig-CAMs adopt. The complex of the mouse junction adhesion molecule-

D1s can functionally replace the D1s for SYG-1 and SYG-2 in 25% of animals (p > 0.001) (Figure 7C). The rescue observed is similar to rescue by Rst/SNS and Neph1/Nephrin chimeras (Figure S6A), and this relatively efficient rescue occurs despite
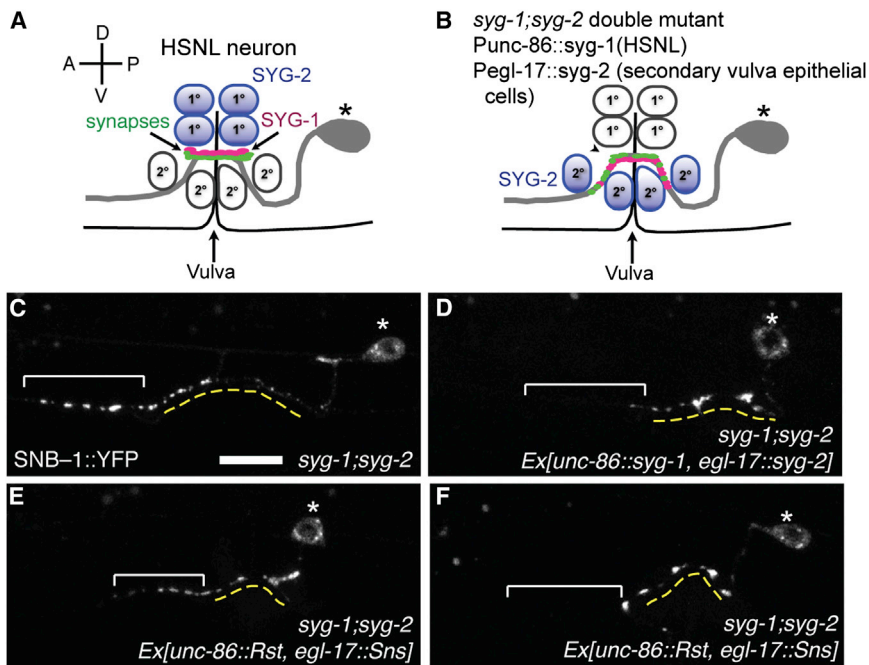
**Figure 6. SYG-1 and SYG-2 D1s Can Be Replaced with Orthologous Domains to Partially Rescue the *syg-1;syg-2* Double-Mutant Defects**

(A) Schematic representation of HSNL synapses at the vulva in wild-type worms, in which SYG-2 is expressed in primary vulval epithelial cells.

(B) Schematic representation of HSNL synapses at the vulva in *syg-1;syg-2* double-mutant worms coinjected with *syg-1* under the control of *unc-86* promoter and *syg-2* under the control of *egl-17* promoter. Because the *egl-17* promoter drives *syg-2* expression in secondary vulval epithelial cells, a wider region for synaptic vesicle clustering is observed.

(C) *syg-1;syg-2* worms show synaptic vesicles in the ectopic anterior region. The dashed yellow line denotes the extent of the secondary cells. The bracket highlights ectopic clustering of SNB-1 in the anterior axon.

(D) Coinjection of *syg-1;syg-2* animals with *Punc86::syg-1* and *Pegl-17::syg-2* results in clustering of synaptic vesicles around the vulva, as explained in (B). Injection of *syg-1* alone fails to rescue the synapses in the *syg-1;syg-2* mutant (Figure 6A).

(E and F) Coinjection of *syg-1* in which its D1 is replaced with D1 of Rst and *syg-2* in which its D1 is replaced with D1 of SNS rescues synaptic defects in some animals (F), but not in others (E). Rescue in (F) resembles that in (D).

See also Figure S6.

the 9-fold weaker affinity of the CAR-JAML interaction versus that of SYG-1-SYG-2. The CD47-Sirpα chimeras, however, did not rescue appreciably (8%) despite having an affinity nearly identical to the SYG-1-SYG-2 interaction (Figure 7B). Interestingly, we could recover function, as indicated by improved rescue (35%), when we replaced the wild-type CD47/Sirpα chimeras with an engineered variant of Sirpα, termed FD6, that binds to CD47 with ~10,000-fold higher affinity than the wild-type protein (Weiskopf et al., 2013). Thus, it appears that the incompatible interaction geometry can be compensated, and overcome, to some degree, with sufficiently high affinity to compel an interaction. That the rescue is incomplete, despite such high affinity, supports the idea that the orthogonal architecture of the SYG-1/SYG-2 complex plays a specific "instructive" role in *C. elegans* synaptogenesis and that this adhesion event is not structurally permissive. This instructive role may be a direct result of the orthogonal architecture on signaling or an indirect consequence of changes in the cell-cell spacing distance with alternative receptor-ligand docking geometries.

To confirm that the chimeric proteins are expressed and targeted to the cell surface, we coinjected *syg-1 syg-2* double-mutant animals with chimeric SYG-1::GFP and SYG-2 pairs. All tested SYG-1 chimeras robustly localized to HSN axons, suggesting that they expressed and folded well (Figure 7D). Those SYG-1/SYG-2 chimeric pairs that rescued the synaptogenesis phenotype also displayed enrichment of SYG-1::GFP in the axonal segment contacting vulval cells, suggesting that the chimeric SYG-2 binding partners are also expressed and folded.

To test whether rigidity of the SYG ectodomains was important for function, we created SYG-1 and SYG-2 variants with ten-residue flexible linkers inserted at two domain boundaries downstream of the interacting domains (between D1 and D2 for both, between D2 and D3 for SYG-1, and between D4 and D5 for SYG-2). When coinjected into *syg-1 syg-2* double mutants, these proteins could not functionally replace rigid SYG-1 and SYG-2 completely, with rescue in 30% of animals (Figure 7C). Similar to the chimeras, we showed that the flexible SYG-1 localized to axons, indicating expression and correct folding. Intriguingly, this partial rescue was not accompanied by enrichment at the vulva (Figure 7D6), raising the possibility that the rigid structure of the SYG extracellular complexes might contribute to the high-density packing of SYG-1 observed near the HSN vulval synapses. Overall, these results indicate that the rigid architecture of the SYG complex may also be required for formation of productive adhesion structures into an interaction plane, leading to synaptogenesis.

## DISCUSSION

The question we address in this study is the role of structure and biophysical interaction parameters between an adhesive receptor-ligand pair in specifying function. It is unclear for most receptors whether extracellular engagement or ligand-induced multimerization alone is sufficient for function or if the unique structural and physical-chemical features of particular systems influence proper functional consequences. This issue is especially pertinent to CAMs, which generally cluster at adhesive sites, raising the question whether structure serves a more specific functional role than establishing a patch of "molecular velcro."
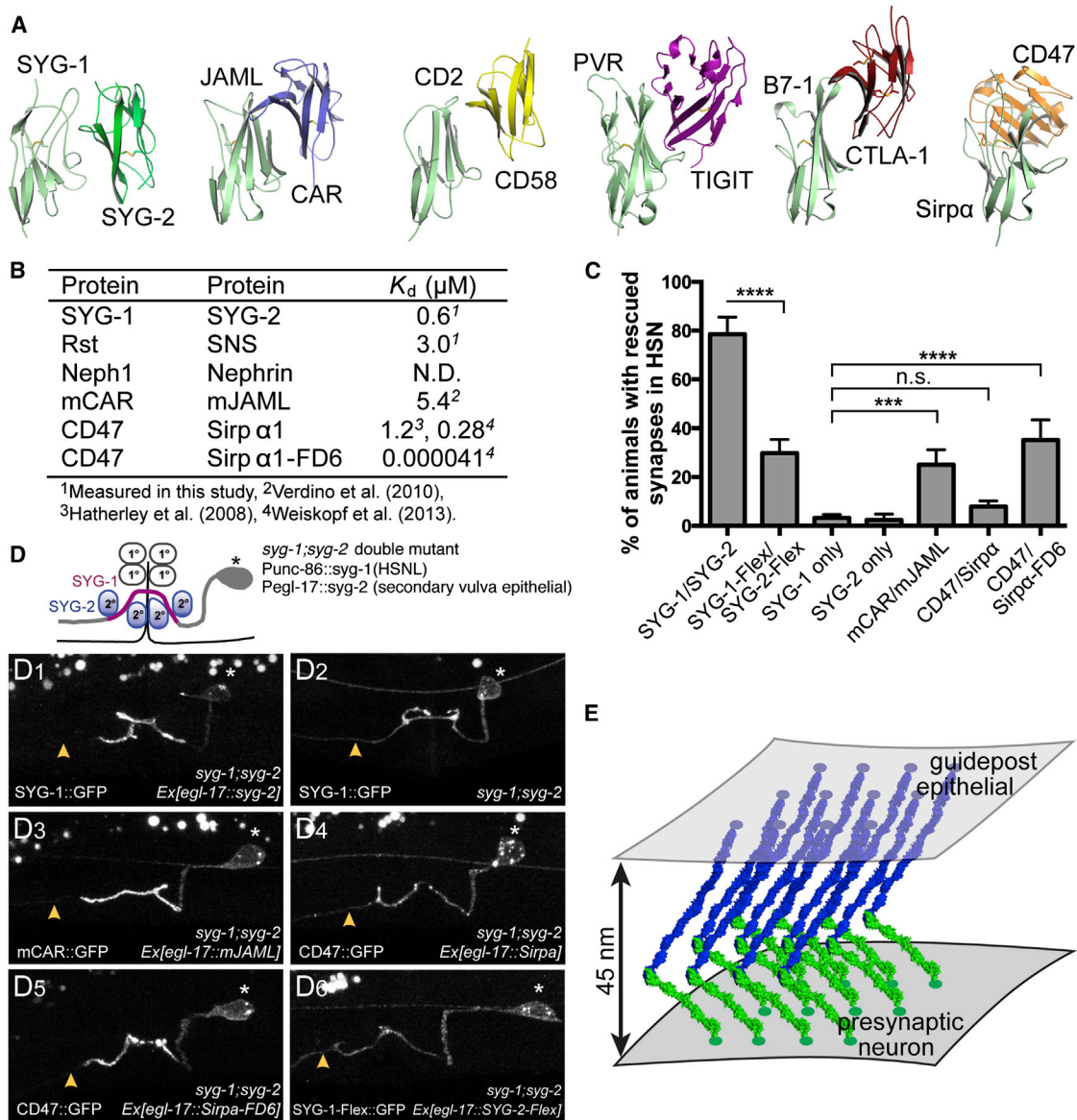
**Figure 7. Rescue Efficiency of *syg-1;syg-2* Double-Mutant Defects Depends on the Geometry and Rigidity of the Interacting Ectodomains**

(A) Comparison of SYG-1/SYG-2 with known structures of Ig-CAM heterocomplexes, all mediated through D1 domains. The structures are ordered from left to right in terms of decreasing similarity to SYG-1/SYG-2 with regards to the approach geometry, where the mouse JAML/CAR complex is most similar to, and the CD47/Sirpα complex is the most different from the SYG-1/SYG-2 complex.

(B) A guide to affinities between the studied complexes as dissociation constants (in μM).

(C) Quantitation of rescue (as phenotype scores) of *syg-1;syg-2* worms when D1s are replaced by D1 domains from indicated proteins. ***p < 0.001 and ****p < 0.0001; n.s., not significant. CAR/JAML D1s can partially rescue *syg-1;syg-2*, but the geometrically different CD47/Sirpα cannot. Lack of CD47/Sirpα can be, however, ameliorated when an extremely high-affinity variant of Sirpα (FD6) is used. Also included is rescue with SYG-1 and SYG-2 modified with flexible interdomain linkers (SYG-1-Flex/SYG-2-Flex), which is significantly diminished compared to rigid WT SYG-1/SYG-2. The error bars represent SD for rescues from three to four independent lines.

(D) Representative images of the localization of SYG-1 chimeras and the flexible SYG-1 variant. For chimeras, SYG-1 D1 domains were replaced with those from other Ig-CAM interactions. SYG-1 constructs have been tagged with a C-terminal GFP and expressed in *syg-1 syg-2* double-mutant background together with the corresponding untagged SYG-2 chimera binding partner in the secondary vulva epithelial cells.

(D1) Enrichment of WT SYG-1::GFP to the axonal regions in contact with SYG-2 expressing secondary vulva epithelial cell. The axon segment anterior to the synaptic region is devoid of SYG-1::GFP staining as denoted by yellow arrow.

(D2) SYG-1::GFP expression alone without SYG-2 is diffusely localized along the entire axon.

(D3) mCAR-SYG-1::GFP and mJAML-SYG-2, which has similar approach geometry as SYG-1 and SYG-2, shows proper localization and enrichment suggestive of binding.

## Roles for Affinity, Biophysical, and Structural Properties in the SYG Complexes

Here, we interrogated this issue in a large family of multipurpose Ig-CAMs that mediate remarkably diverse functions such as synaptogenesis, myoblast fusion, axon guidance, and formation of the kidney filtration barrier. We found that homophilic and heterophilic complexes of SYG-1 and SYG-2 orthologs engage one another through an evolved dual specificity so as to have the capacity to form homophilic and heterophilic complexes. Furthermore, we demonstrated that the residues critically involved in the SYG-1-SYG-2 interface mediate an interaction affinity that is ideal for proper synaptogenesis in *C. elegans*. In this way, the specific binding chemistry mediates an interaction affinity that has been fine-tuned for function. Remarkably, the interaction domains—D1s of SYG-1 and SYG-2—could be functionally replaced with orthologous domains from *Drosophila* and mouse and even with domains from an unrelated Ig-CAM complex (JAML-CAR) as long as the complexes had a similar docking geometry to the SYG-1/SYG-2 complex. However, another Ig-CAM complex with a substantially different interaction geometry, CD47-Sirpα, failed to functionally rescue the *syg1;syg-2* phenotype. Furthermore, increasing the flexibility of the SYG ectodomains through the insertion of Gly-Ser linkers also lead to decreased rescue. Our work suggests that functional signaling initiated by SYG-like proteins is critically linked to the architecture and physical chemistry of the extracellular interactions, and thus these parameters play "instructive" roles in function.

Structural rigidity of adhesion molecules might have specific functional significance in diverse biological contexts. For example, the rigid tip-link adhesion complexes formed by cadherin molecules Pcdh15 and Pchd23 might be necessary to transform force into intracellular signaling (Sotomayor et al., 2012). Cadherins require calcium for rigidifying their ectodomains (Shapiro and Weis, 2009), which then protrude and are primed for *trans* interactions and cell-cell adhesion. The rigidity observed may also be a factor allowing close packing of SYG complexes into a dense matrix within an interaction plane, facilitating downstream signaling through juxtamembrane recruitment of proteins and cytoskeleton.

Other cell-surface receptor-ligand systems, such as cytokine or tyrosine-kinase receptors for soluble growth factors, are activated through soluble ligand-induced oligomerization. CAMs, on the other hand, are composed of interactions between two cell-associated membrane proteins that span an intercellular adhesive junction that, in most cases, is composed of tightly packed complexes (for example, Al-Amoudi et al., 2007). The surprising sensitivity of the SYG-1/SYG-2 complex geometry on preservation of its docking mode suggests a possible dependency on complex architecture within dense adhesive junctions to allow close packing of individual complexes to achieve not only the high-density packing of receptors but also the highly regular subsynaptic spatial specifications. Interestingly, the prefusion complex during myoblast fusion, another SYG family protein-mediated adhesion complex, was described as dense membrane plaques between apposed cells under EM, suggesting that this type of adhesion molecule effectively concentrates intracellular proteins.

Our results also link SYGs to another Ig-CAM family of proteins that exhibits homo- and heterophilic adhesion properties, the nectins and nectin-like proteins (Harrison et al., 2012). In this family of nine related proteins, heterophilic binding is consistently higher affinity than homophilic binding, similar to SYG-1- and SYG-2-like proteins. For nectins, crystal structures have now demonstrated conserved modes of binding between homophilic and heterophilic interactions utilizing the same interface on the C′CFG face of the N-terminal immunoglobulin domains.

## Structural Features of SYGs Determine Functional Properties of Their Cellular Adhesions

Our structural results are pertinent to many diverse SYG-mediated cell adhesions. As mentioned, the slit diaphragm of the kidney, which serves to filter blood, is constructed by SYG orthologs Neph1 and Nephrin. The thickness of the slit diaphragm has been measured to be ~40 Å (Haraldsson et al., 2008). Our complex model with elongated subunits and orthogonal interaction geometry, based on our crystal structure and EM data, span 40 to 50 Å (Figure 7E) and are therefore consistent with the physiological distances measured for the slit diaphragm. Collectively, the insight we have gained into how the biophysical features of SYGs impact function will help to explain the functional architecture of the myriad of other known SYG-mediated cellular adhesions.

### EXPERIMENTAL PROCEDURES

#### Protein Expression and Purification

All SYG-1, SYG-2, and orthologs, unless stated otherwise, were expressed using baculoviruses and High Five cells (Invitrogen) from *Trichoplusia ni* by secretion into culture media as C-terminal hexahistidine-tagged proteins. SYG-2 D4 was expressed in High Five cells as an HRV 3C Protease-cleavable N-terminal hexahistidine- and Fc-fusion. Proteins were purified using nickel-nitrilotriacetic acid agarose resin (QIAGEN) and size exclusion chromatography in 10 mM HEPES (pH 7.2), 150 mM NaCl. For selenomethionine labeling in bacteria, SYG-1 D1D2 was also refolded from inclusion bodies obtained by cytoplasmic expression in B834(DE3) cells (EMD Millipore).

#### Biophysical Studies of Protein Interactions

SPR experiments were performed with streptavidin (SA) chips using a Biacore T100 or 3000 (GE Healthcare). Proteins to be captured on SA chips were biotinylated at their C termini using the *E. coli* biotin ligase BirA. Isothermal titration calorimetry experiments were done using a Microcal VP-ITC (GE Healthcare).

#### Crystallography of SYG-1, SYG-2, and Their Orthologs

SYG-1 was phased using multiple-wavelength anomalous diffraction methods with selenomethionine-labeled D1D2 crystals. Other SYG-1-like structures

(D4) CD47-SYG-1::GFP and Sirpa-SYG-2 with dissimilar approach geometry fails to localize and is found diffused along the entire axon.

(D5) Sirpa-FD6-SYG-2, which has very high affinity for CD47::GFP, results in the subcellular enrichment of CD47::GFP.

(D6) Flexible SYG-1 (SYG-1-Flex::GFP) is found diffused along the entire axon, which is indicative of proper expression and targeting to the membrane but is not enriched where SYG-2-Flex is expressed.

(E) Suggested cellular adhesion model involving SYG-1 (green) and SYG-2 (blue).

were solved by using the SYG-1 D1D2 structure as a molecular replacement model. SYG-2 D4 structure was solved using tantalum bromide cluster derivatives and the single-wavelength anomalous diffraction method. SYG-1/SYG-2 crystals could be grown using the N391C mutant of SYG-2, which removed an N-linked glycosylation site. The heterophilic complex was solved by a combination of molecular replacement with SYG-1 and SYG-2 D4, followed by manual rebuilding of all other domains, which was aided by homology modeling with Modeler (Eswar et al., 2006) and our SYG-2 D3D4 structure.

All structural models were built and refined using Coot (Emsley et al., 2010) and Phenix.refine (Adams et al., 2010). Structure validation was performed by tools available within Coot and the PHENIX suit, mostly using Molprobity (Chen et al., 2010). For the mouse Neph1 D1-D2 structure, due to low resolution of the data, we refined the molecular replacement model by further creating homology models in Modeler (Eswar et al., 2006), followed by dynamic elastic network refinement in CNS (Schröder et al., 2007).

### Electron Microscopy and Image Processing

Purified SYG-1 and SYG-2 and crosslinked SYG-1/SYG-2 complex were prepared by conventional negative staining with 0.75% uranyl formate (Ohi et al., 2004), and images were recorded on a Tecnai T12 microscope (FEI) at a nominal magnification of 42,000× with a defocus value of −1.5 μm. Particles were selected using BOXER, part of the EMAN2 software package (Tang et al., 2007), and were processed using SPIDER (Frank et al., 1996).

### *C. elegans* Strains

All worm strains were maintained at 20°C on OP50 *E. coli*-seeded nematode growth medium plates. N2 Bristol stain worms were used as the wild-type reference, and the following mutants were used: *syg-1(ky652)X* and *syg-2 (ky673)X*. See the Extended Experimental Procedures for transgenic lines used in this study. Expression plasmids for transgenic worm lines were made using the pSM vector, a derivative of pPD49.26 (A. Fire). Plasmids were injected into animals at 1 ng/μl for the *unc-86* promoter and 15 ng/μl for the *egl-17* promoter together with coinjection markers *Podr-1::gpf* or *Podr-1::dsred* at 20 ng/μl.

### Fluorescence Quantification and Confocal Imaging

All fluorescence images of HSNL synapses in L4 or young adults were taken with a 63× objective on a Zeiss Axioplan 2 Imaging System or a Plan-Apochromat 63×/1.4 objective on a Zeiss LSM710 confocal microscope. Total fluorescence intensity was determined using Image J software (NIH) by summing pixel intensity, and the average fluorescence intensity was calculated for each group (n = 10).

### ACCESSION NUMBERS

The coordinates and structure factors for the reported crystal structures are deposited in the Protein Data Bank (PDB) under PDB IDs 4OF0, 4O43, 4OF6, 4OF7, 4OF8, 4OFD, 4OFI, 4OFK, 4OFP, and 4OFY.

### SUPPLEMENTAL INFORMATION

Supplemental Information includes Extended Experimental Procedures, six figures, and two tables and can be found with this article online at http://dx.doi.org/10.1016/j.cell.2014.01.004.

### REFERENCES

Abmayr, S.M., and Pavlath, G.K. (2012). Myoblast fusion: lessons from flies and mice. Development *139*, 641–656.

Adams, P.D., Afonine, P.V., Bunkóczi, G., Chen, V.B., Davis, I.W., Echols, N., Headd, J.J., Hung, L.-W., Kapral, G.J., Grosse-Kunstleve, R.W., et al. (2010). PHENIX: a comprehensive Python-based system for macromolecular structure solution. Acta Crystallogr. D Biol. Crystallogr. *66*, 213–221.

Al-Amoudi, A., Díez, D.C., Betts, M.J., and Frangakis, A.S. (2007). The molecular architecture of cadherins in native epidermal desmosomes. Nature *450*, 832–837.

Bao, S., and Cagan, R. (2005). Preferential adhesion mediated by Hibris and Roughest regulates morphogenesis and patterning in the Drosophila eye. Dev. Cell *8*, 925–935.

Bork, P., Holm, L., and Sander, C. (1994). The immunoglobulin fold. Structural classification, sequence patterns and common core. J. Mol. Biol. *242*, 309–320.

Boschert, U., Ramos, R.G., Tix, S., Technau, G.M., and Fischbach, K.F. (1990). Genetic and developmental analysis of irreC, a genetic function required for optic chiasm formation in Drosophila. J. Neurogenet. *6*, 153–171.

Chao, D.L., and Shen, K. (2008). Functional dissection of SYG-1 and SYG-2, cell adhesion molecules required for selective synaptogenesis in C. elegans. Mol. Cell. Neurosci. *39*, 248–257.

Chen, V.B., Arendall, W.B., 3rd, Headd, J.J., Keedy, D.A., Immormino, R.M., Kapral, G.J., Murray, L.W., Richardson, J.S., and Richardson, D.C. (2010). MolProbity: all-atom structure validation for macromolecular crystallography. Acta Crystallogr. D Biol. Crystallogr. *66*, 12–21.

Chia, P.H., Patel, M.R., and Shen, K. (2012). NAB-1 instructs synapse assembly by linking adhesion molecules and F-actin to active zone proteins. Nat. Neurosci. *15*, 234–242.

Ding, M., Chao, D., Wang, G., and Shen, K. (2007). Spatial regulation of an E3 ubiquitin ligase directs selective synapse elimination. Science *317*, 947–951.

Dworak, H.A., Charles, M.A., Pellerano, L.B., and Sink, H. (2001). Characterization of Drosophila hibris, a gene related to human nephrin. Development *128*, 4265–4276.

Emsley, P., Lohkamp, B., Scott, W.G., and Cowtan, K. (2010). Features and development of Coot. Acta Crystallogr. D Biol. Crystallogr. *66*, 486–501.

Eswar, N., Webb, B., Marti-Renom, M.A., Madhusudhan, M.S., Eramian, D., Shen, M.-Y., Pieper, U., and Sali, A. (2006). Comparative protein structure modeling using Modeller. Curr. Protoc. Bioinformatics *15*, 5.6.1–5.6.30.

Frank, J., Radermacher, M., Penczek, P., Zhu, J., Li, Y., Ladjadj, M., and Leith, A. (1996). SPIDER and WEB: processing and visualization of images in 3D electron microscopy and related fields. J. Struct. Biol. *116*, 190–199.

Galletta, B.J., Chakravarti, M., Banerjee, R., and Abmayr, S.M. (2004). SNS: Adhesive properties, localization requirements and ectodomain dependence in S2 cells and embryonic myoblasts. Mech. Dev. *121*, 1455–1468.

Gerke, P., Huber, T.B., Sellin, L., Benzing, T., and Walz, G. (2003). Homodimerization and heterodimerization of the glomerular podocyte proteins nephrin and NEPH1. J. Am. Soc. Nephrol. *14*, 918–926.

Haraldsson, B., Nyström, J., and Deen, W.M. (2008). Properties of the glomerular barrier and mechanisms of proteinuria. Physiol. Rev. *88*, 451–487.

Harrison, O.J., Vendome, J., Brasch, J., Jin, X., Hong, S., Katsamba, P.S., Ahlsen, G., Troyanovsky, R.B., Troyanovsky, S.M., Honig, B., and Shapiro, L. (2012). Nectin ectodomain structures reveal a canonical adhesive interface. Nat. Struct. Mol. Biol. *19*, 906–915.

Hatherley, D., Graham, S.C., Turner, J., Harlos, K., Stuart, D.I., and Barclay, A.N. (2008). Paired receptor specificity explained by structures of signal regulatory proteins alone and complexed with CD47. Mol. Cell *31*, 266–277.

Huber, T.B., Schmidts, M., Gerke, P., Schermer, B., Zahn, A., Hartleben, B., Sellin, L., Walz, G., and Benzing, T. (2003). The carboxyl terminus of Neph family members binds to the PDZ domain protein zonula occludens-1. J. Biol. Chem. *278*, 13417–13421.

Hynes, R.O., and Zhao, Q. (2000). The evolution of cell adhesion. J. Cell Biol. *150*, F89–F96.

Jones, N., Blasutig, I.M., Eremina, V., Ruston, J.M., Bladt, F., Li, H., Huang, H., Larose, L., Li, S.S.-C., Takano, T., et al. (2006). Nck adaptor proteins link nephrin to the actin cytoskeleton of kidney podocytes. Nature *440*, 818–823.

Kestilä, M., Lenkkeri, U., Männikkö, M., Lamerdin, J., McCready, P., Putaala, H., Ruotsalainen, V., Morita, T., Nissinen, M., Herva, R., et al. (1998). Positionally cloned gene for a novel glomerular protein—nephrin—is mutated in congenital nephrotic syndrome. Mol. Cell *1*, 575–582.

Khoshnoodi, J., Sigmundsson, K., Ofverstedt, L.-G., Skoglund, U., Obrink, B., Wartiovaara, J., and Tryggvason, K. (2003). Nephrin promotes cell-cell adhesion through homophilic interactions. Am. J. Pathol. *163*, 2337–2346.

Liu, G., Kaw, B., Kurfis, J., Rahmanuddin, S., Kanwar, Y.S., and Chugh, S.S. (2003). Neph1 and nephrin interaction in the slit diaphragm is an important determinant of glomerular permeability. J. Clin. Invest. *112*, 209–221.

Mizuhara, E., Minaki, Y., Nakatani, T., Kumai, M., Inoue, T., Muguruma, K., Sasai, Y., and Ono, Y. (2010). Purkinje cells originate from cerebellar ventricular zone progenitors positive for Neph3 and E-cadherin. Dev. Biol. *338*, 202–214.

Neumann-Haefelin, E., Kramer-Zucker, A., Slanchev, K., Hartleben, B., Noutsou, F., Martin, K., Wanner, N., Ritter, A., Gödel, M., Pagel, P., et al. (2010). A model organism approach: defining the role of Neph proteins as regulators of neuron and kidney morphogenesis. Hum. Mol. Genet. *19*, 2347–2359.

Ohi, M., Li, Y., Cheng, Y., and Walz, T. (2004). Negative staining and image classification – powerful tools in modern electron microscopy. Biol. Proced. Online *6*, 23–34.

Özkan, E., Carrillo, R.A., Eastman, C.L., Weiszmann, R., Waghray, D., Johnson, K.G., Zinn, K., Celniker, S.E., and Garcia, K.C. (2013). An extracellular interactome of immunoglobulin and LRR proteins reveals receptor-ligand networks. Cell *154*, 228–239.

Ramos, R.G., Igloi, G.L., Lichte, B., Baumann, U., Maier, D., Schneider, T., Brandstätter, J.H., Fröhlich, A., and Fischbach, K.F. (1993). The irregular chiasm C-roughest locus of Drosophila, which affects axonal projections and programmed cell death, encodes a novel immunoglobulin-like protein. Genes Dev. *7* (12B), 2533–2547.

Schneider, T., Reiter, C., Eule, E., Bader, B., Lichte, B., Nie, Z., Schimansky, T., Ramos, R.G., and Fischbach, K.F. (1995). Restricted expression of the irreC-rst protein is required for normal axonal projections of columnar visual neurons. Neuron *15*, 259–271.

Schröder, G.F., Brunger, A.T., and Levitt, M. (2007). Combining efficient conformational sampling with a deformable elastic network model facilitates structure refinement at low resolution. Structure *15*, 1630–1641.

Serizawa, S., Miyamichi, K., Takeuchi, H., Yamagishi, Y., Suzuki, M., and Sakano, H. (2006). A neuronal identity code for the odorant receptor-specific and activity-dependent axon sorting. Cell *127*, 1057–1069.

Shapiro, L., and Weis, W.I. (2009). Structure and biochemistry of cadherins and catenins. Cold Spring Harb. Perspect. Biol. *1*, a003053.

Shelton, C., Kocherlakota, K.S., Zhuang, S., and Abmayr, S.M. (2009). The immunoglobulin superfamily member Hbs functions redundantly with Sns in

interactions between founder and fusion-competent myoblasts. Development *136*, 1159–1168.

Shen, K., and Bargmann, C.I. (2003). The immunoglobulin superfamily protein SYG-1 determines the location of specific synapses in C. elegans. Cell *112*, 619–630.

Shen, K., Fetter, R.D., and Bargmann, C.I. (2004). Synaptic specificity is generated by the synaptic guidepost protein SYG-2 and its receptor, SYG-1. Cell *116*, 869–881.

Sohn, R.L., Huang, P., Kawahara, G., Mitchell, M., Guyon, J., Kalluri, R., Kunkel, L.M., and Gussoni, E. (2009). A role for nephrin, a renal protein, in vertebrate skeletal muscle cell fusion. Proc. Natl. Acad. Sci. USA *106*, 9274–9279.

Sotomayor, M., Weihofen, W.A., Gaudet, R., and Corey, D.P. (2012). Structure of a force-conveying cadherin bond essential for inner-ear mechanotransduction. Nature *492*, 128–132.

Tang, G., Peng, L., Baldwin, P.R., Mann, D.S., Jiang, W., Rees, I., and Ludtke, S.J. (2007). EMAN2: an extensible image processing suite for electron microscopy. J. Struct. Biol. *157*, 38–46.

Venugopala Reddy, G., Reiter, C., Shanbhag, S., Fischbach, K.F., and Rodrigues, V. (1999). Irregular chiasm-C-roughest, a member of the immunoglobulin superfamily, affects sense organ spacing on the Drosophila antenna by influencing the positioning of founder cells on the disc ectoderm. Dev. Genes Evol. *209*, 581–591.

Verdino, P., Witherden, D.A., Havran, W.L., and Wilson, I.A. (2010). The molecular interaction of CAR and JAML recruits the central cell signal transducer PI3K. Science *329*, 1210–1214.

Verma, R., Kovari, I., Soofi, A., Nihalani, D., Patrie, K., and Holzman, L.B. (2006). Nephrin ectodomain engagement results in Src kinase activation, nephrin phosphorylation, Nck recruitment, and actin polymerization. J. Clin. Invest. *116*, 1346–1359.

Vishnu, S., Hertenstein, A., Betschinger, J., Knoblich, J.A., Gert de Couet, H., and Fischbach, K.-F. (2006). The adaptor protein X11Lalpha/Dmint1 interacts with the PDZ-binding domain of the cell recognition protein Rst in Drosophila. Dev. Biol. *289*, 296–307.

Völker, L.A., Petry, M., Abdelsabour-Khalaf, M., Schweizer, H., Yusuf, F., Busch, T., Schermer, B., Benzing, T., Brand-Saberi, B., Kretz, O., et al. (2012). Comparative analysis of Neph gene expression in mouse and chicken development. Histochem. Cell Biol. *137*, 355–366.

Wanner, N., Noutsou, F., Baumeister, R., Walz, G., Huber, T.B., and Neumann-Haefelin, E. (2011). Functional and spatial analysis of C. elegans SYG-1 and SYG-2, orthologs of the Neph/nephrin cell adhesion module directing selective synaptogenesis. PLoS ONE *6*, e23598.

Weavers, H., Prieto-Sánchez, S., Grawe, F., Garcia-López, A., Artero, R., Wilsch-Bräuninger, M., Ruiz-Gómez, M., Skaer, H., and Denholm, B. (2009). The insect nephrocyte is a podocyte-like cell with a filtration slit diaphragm. Nature *457*, 322–326.

Weiskopf, K., Ring, A.M., Ho, C.C.M., Volkmer, J.-P., Levin, A.M., Volkmer, A.K., Ozkan, E., Fernhoff, N.B., van de Rijn, M., Weissman, I.L., and Garcia, K.C. (2013). Engineered SIRPα variants as immunotherapeutic adjuvants to anticancer antibodies. Science *341*, 88–91.

Wolff, T., and Ready, D.F. (1991). Cell death in normal and rough eye mutants of Drosophila. Development *113*, 825–839.

Yamagata, M., Sanes, J.R., and Weiner, J.A. (2003). Synaptic adhesion molecules. Curr. Opin. Cell Biol. *15*, 621–632.

## EXTENDED EXPERIMENTAL PROCEDURES

### Protein Expression and Purification

All proteins, unless indicated otherwise, were expressed using baculoviruses. Protein constructs were fused to C-terminal hexahistidine tags for facile purification with immobilized metal affinity chromatography (IMAC) using Nickel-Nitriloacetic acid (Ni-NTA) Agarose resin (QIAGEN, 30230). Constructs of interest were cloned into pAcGP67A (BD Biosciences, 554759), and baculoviruses were created by co-transfections with BaculoGold (BD Biosciences, 560129) into Sf9 cells (*Spodoptera frugiperda*) using Cellfectin II (Invitrogen, 10362-100). Proteins were expressed by secretion to culture media, Insect-XPRESS (Lonza, 12-730Q), from High Five cells (*Trichoplusia ni*). Expression media were collected 48-72 hr post-infection, and mixed with 50 mM Tris pH 8.0, 5 mM $CaCl_2$, 1 mM $NiCl_2$ (final concentrations) at room temperature. After separating the precipitate via centrifugation, hexahistidine-tagged proteins were captured using Ni-NTA Agarose, washed with 10 mM HEPES pH 7.2, 150 mM NaCl (HEPES-Buffered Saline, HBS) including 20 mM Imidazole, pH 7.2, and eluted with HBS with 200 mM Imidazole. The protein samples were further purified by gel filtration chromatography using Superdex 75 or Superdex 200 columns (GE Healthcare, 17-1047-01 and 17-1088-01) in HBS.

For the purification of SYG-2 D1-D4, instead of the $Ni^{2+}/Ca^{2+}$ precipitation before the IMAC, we used a Centramate tangential flow concentrator (PAL Corporation) to exchange media with HBS, since this improved protein yield approximately five fold.

For expression of SYG-2 D4, we used an N-terminal hexahistidine and Fc (crystallizable fragment of human IgG1) fusion construct for expression using baculovirus. The N-terminal Fc fusion was necessary for producing folded SYG-2 D4. SYG-2 D4 was freed from the N-terminal tags using an engineered HRV 3C Protease site.

For the production of SYG-1/SYG-2 complexes, we co-infected High Five cells with both SYG-1 and SYG-2 baculoviruses. The complexes could be separated from excess SYG-1 over Superdex 200 gel filtration columns.

For efficient selenomethionine (SeMet) labeling and eventual phasing of crystal structures, we also produced the first two domains of SYG-1 (SYG-1 D1D2) in *E. coli* as inclusion bodies. SYG-1 D1D2 was cloned into pHis-parallel1 (Sheffield et al., 1999), which encodes for a TEV protease-cleavable N-terminal hexahistidine fusion, and was expressed in BL21(DE3) in LB medium for native-like expression, or in B834(DE3) cells (EMD Millipore, 69041) with minimal medium including L-Selenomethionine for expression of SeMet-labeled protein (Doublié, 2007). Native and SeMet-labeled SYG-1 D1D2 were successfully refolded using a protocol previously published for peptide-MHC complexes (Garboczi et al., 1992, 1996). Briefly, inclusion bodies were dissolved in 50 mM MES pH 6, 8 M Urea and 0.1 mM DTT, and refolded by quick dilution in 100 mM Tris pH 8, 400 mM L-Arginine, 0.5 mM oxidized glutathione, 5 mM reduced glutathione and protease inhibitors. The refolded protein was dialyzed against 20 mM Tris pH 8.0 and 150 mM NaCl, captured by Ni-NTA resin, cleaved with TEV protease, and purified over a Superdex 75 gel filtration column in HBS.

For capturing proteins on streptavidin-coupled surfaces used in surface plasmon resonance experiments, we also generated baculoviruses expressing proteins with C-terminal biotinylation and hexahistidine tags. For production of these proteins, High Five cells were co-infected with baculovirus expressing the *E. coli* enzyme BirA in a secreted form, and media were supplemented with 100 μM D-Biotin. Biotinylated protein purification was done as above without any modifications.

### Protein Biophysics: Isothermal Titration Calorimetry, Surface Plasmon Resonance, and Multiangle Light Scattering

All Isothermal Titration Calorimetry (ITC) and Multi-Angle Light Scattering (MALS) experiments were done in HBS. Surface Plasmon Resonance (SPR) was performed in HBSp+ (HBS + 0.05% Surfactant P20, pH 7.4; GE Healthcare, BR-1006-71) with Bovine Serum Albumin (BSA), which was added to ameliorate non-specific interactions with carboxymethyldextran-based SPR chips. For the *C. elegans* SYG-1 and SYG-2, we used 0.1% BSA, and for the *Drosophila* orthologs, we used 1% BSA. ITC was performed at 27°C, while SPR and MALS experiments were done at 25°C.

ITC was performed using a Microcal VP-ITC (GE Healthcare), and data analysis was done in a modified version of Origin version 7d, using the single-binding site model.

SPR was performed using a Biacore T100 (GE Healthcare), with streptavidin-coated sensor chips (SA chips, GE Healthcare, BR-1005-31). For all interactions between SYG-1 and SYG-2 orthologs, kinetics of binding were too fast to measure ($k_{off} \geq 0.5 \text{ s}^{-1}$), and therefore only dissociation constants measured through steady-state binding responses are reported. SPR data were fit using a simple Langmuir isotherm model. For very low affinity interactions (such as SYG-1 F60A, double and triple SYG-1 mutants), the full response ($R_{max}$) was estimated based on measured responses to higher-affinity mutants tested on the same chip surface. In all the cases in which saturation could be achieved in titration experiments, calculated $R_{max}$ values were $\geq 50\%$, and usually around 70% of theoretical $R_{max}$ values, based on surface-captured biotinylated ligand. This high ratio of active surface protein is due to non-random, directional capture on streptavidin-coated chips, where the C-terminal end of SYG-1 and SYG-2 orthologs are captured, and N-terminal domains are successfully presented.

MALS was performed using a combination of gel filtration chromatography with a Shodex Protein KW-803 column (Showa Denko), coupled to a Dawn EOS Refractometer and an 18-angle Optilab light scattering detector (Wyatt Technology). For calculation of molar mass, estimated *dn/dc* values were used due to N-linked glycosylation of SYG-1 and SYG-2. These were 0.173 for SYG-1 ectodomain and 0.174 for the SYG-1/SYG-2 ectodomain complex, based on predicted glycosylation content of the proteins. Calculated molecular weights for our hexahistidine-tagged SYG-1 and SYG-2 ectodomains are 60.45 kDa and 113.07 kDa, respectively. When predicted N-linked glycosylations are added, the estimated molecular weights increase to ~83 kDa (SYG-1) and ~146 kDa

(SYG-2), with the complex being ∼229 kDa, closely matching molar masses measured with MALS for free SYG-1 and the SYG-1/SYG-2 complex ECDs (Figure S4G).

## Protein Crystallization

Protein crystal screening was done using Mosquito (TTP Labtech) and Phoenix (Art Robbins) crystallization robots usually at 100 nl +100 nl protein:crystallant ratios, in a sitting drop, vapor diffusion setting against 60 μl of crystallant. Initial crystal leads were obtained using crystallization screens from Hampton Research, Emerald Biosciences and Molecular Dimensions. All crystals were grown at 22°C with proteins at 15 to 25 mg/ml concentrations.

The crystallization and cryoprotection conditions for protein structures reported here are as follows:

- SYG-1 D1D2 expressed in High Five cells, which resulted in N-linked glycosylation, crystallized in 25% Polyethylene glycol (PEG) 200, 5% PEG 3,000, 0.1 M MES pH 6.5. The crystals were cryoprotected by paraffin oil.
- Refolded SYG-1 D1D2, without glycosylation, was crystallized in 20% PEG 3,350, 0.2 M Ammonium acetate, 0.1 M HEPES pH 7.0. The SeMet-labeled crystals could be grown in drops microseeded with native crystals in 18% PEG 3,350, 0.2 M Ammonium acetate, 0.1 M HEPES pH 7.0. These crystals, which were shaped as rods, matured to their largest size in 5 days after setting up of the sitting drops, and consistently disappeared at day 6. The crystal structure, which was solved using three-wavelength MAD, shows that few crystal contacts exist in one direction, which also lead to D1 being mobile and "smearing" of the maps for D1, This is also apparent by the high atomic displacement parameters (B factors) for D1.
- SYG-1 D1 expressed in High Five cells, which resulted in N-linked glycosylation, was crystallized in two different conditions: First was 1.2 M Trisodium citrate, 0.1 M HEPES pH 7.0, and these crystals were cryoprotected with 15% Ethylene glycol. The second crystal form was grown in 32.5% PEG 3,350, 0.2 M Lithium sulfate, 0.1 M Tris pH 8.5, and these crystals were cryoprotected in paraffin oil.
- Rst D1D2 was expressed in High Five cells, but since the amino acid sequence contained no glycosylation motifs, it was not glycosylated. It crystallized initially in 15% PEG 3,350, 0.1 M MES pH 6.5 as small crystal showers, which were used to prepare microseed stocks. These microseeds nucleated larger crystals in 8% PEG 3,350, 0.1 M MES pH 6.5. These crystals were cryoprotected with 25% Glycerol.
- Duf D1 was expressed in High Five cells, which resulted in N-linked glycosylation of the protein. It was crystallized in 25% PEG 3,350, 0.2 M Sodium chloride, 0.1 M Bis-tris pH 5.5, and the crystals were cryoprotected with 25% Glycerol.
- Neph1 D1D2 was expressed in High Five cells, which resulted in N-linked glycosylation of the protein. Its crystals were grown in 15% PEG 3,350, 3% Dextran sulfate, 0.1 M Sodium citrate, pH 5.5, and were cryoprotected in 25% Glycerol.
- The complex of SYG-1 D1D2 and SYG-2 D1-D4 was expressed in High Five cells, with N-linked glycosylation. It was crystallized in 18% PEG 3,350, 2% Acetone, 0.1 M HEPES pH 7.2. These crystals could be cryoprotected in 22% Glycerol. The crystal that was used to determine the structure was grown in the said condition above, but the cryoprotectant had 3% 1,4-Dioxane instead of Acetone, as we had discovered that the two additives were interchangeable for crystal growth and stabilization. These crystals were of low quality overall, and screening hundreds of them revealed only a handful that diffracted to better than 4 Å. Eventually they were not sufficient to solve the phase problem for the SYG-1/SYG-2 complex.
- The complex of SYG-1 D1D2 and SYG-2 D1-D4 with the mutation N391C was among many mutants designed to create mercury derivatives for phasing, and was expressed in High Five cells. By its design, the N-linked glycosylation site N391, which we predicted to be fully accessible, was mutated and replaced with a cysteine. It was derivatized with ethylmercury phosphate in 10 mM HEPES pH 7.2 with no salt added due to the water insolubility of ethylmercury chloride, followed by buffer exchange on PD-10 columns to remove excess ethylmercury. Crystals did not grow in the condition for wild-type SYG-1/SYG-2, but did appear in the related condition, 16% PEG 3,350, 0.2 M Triammonium citrate, 0.1 M MES pH 6.4. Screening of many of these crystals revealed that they were also low quality, but we found one that diffracted to ∼3.3 Å. Unfortunately, due to a failed fluorescence scan, we failed to collect any useful anomalous data. This data set, however, was higher quality and resolution than the wild-type data set, and allowed us to solve the SYG-1/SYG-2 complex structure.
- SYG-2 D4 was expressed in High Five cells as explained above, and was N-glycosylated. It crystallized in 1.3 M Ammonium sulfate, 0.1 M Tris pH 8.3. For phasing, it was derivatized with 0.2 mM $Ta_6Br_{12}^{2+}$ (Jena Bioscience, PK-103) in the mother liquor, which is saturating for the tantalum cluster, for 5 days. We observed crystals turning green over several days and depleting the precipitated cluster from its surrounding. These crystals were cryoprotected with 35% Ethylene glycol.
- SYG-2 D3D4 was co-expressed with secreted Endo H in High Five cells in the presence of 10 μM Kifunensine, which renders N-linked glycosylation Endo H-sensitive, resulting in reduced N-linked glycosylation. Crystals were grown in 0.9 M Diammonium tartrate, 0.1 M Sodium acetate, pH 4.5, and were cryoprotected with 25% Glycerol.

## Crystallography—Structure Determination—Outlines

Crystallographic data were collected at several synchrotron beamlines including Stanford Synchrotron Radiation Laboratory (SSRL) beamlines 11-1, 9-2 and 12-2; Advanced Light Source (ALS) beamlines 8.2.1 and 8.2.2; and Advanced Photon Source (APS) beamline 23-IDb. Data were indexed and scaled with HKL-2000 (Otwinowski and Minor, 1997), XDS (Kabsch, 2010) and HKL-3000 (Minor

et al., 2006). Model refinement was performed by using Phenix.refine (Afonine et al., 2012) within the PHENIX package (Adams et al., 2010), and model building was done using COOT (Emsley et al., 2010). Molprobity (Chen et al., 2010) tools within PHENIX and on-line were used for validation. For phasing, different functions within the CNS (Brunger, 2007), SHARP (Bricogne et al., 2003; Vonrhein et al., 2007) and SHELX (Sheldrick, 2010) packages were utilized. For the more challenging and special cases of structure solution of refolded SYG-1 D1D2, SYG-2 D4, Neph1 D1D2 and the SYG-1/SYG-2 complex, see the specific sections below. Crystallographic data and refinement statistics for all structures reported in this study are tabulated in Table S2.

## Structure Determination of SYG-1

The structure of SeMet-labeled, refolded SYG-1 D1D2 was determined by three-wavelength multi-wavelength anomalous diffraction (MAD) phasing, using SHELX for substructure determination, and SHARP for phase refinement. However, the D1 domain proved difficult to model, as density of ~60% of the model was smeared due to the small swinging motions within the D1 domain, which was not held in place by crystal contacts. The part of the domain that could be confidently determined was between the disulfide linkage and the D2 boundary, suggesting that the coordinated "breathing" and swinging of atoms might be inherent to this Ig domain. To determine an accurate model of SYG-1 D1, we also solved the structure of insect cell-produced SYG-1 D1 in two crystal forms, using the 40% partial D1 model from the refolded SYG-1 D1D2 structure with PHASER (McCoy et al., 2007), where we successfully built the rest of SYG-1 D1. Finally, this structure was used for molecular replacement with PHASER for the determination of the insect-cell produced, glycosylated SYG-1 D1D2. These four structures of SYG-1 do not share unit cell parameters, or have related lattices. Therefore, lack of a common dimeric interface between any of these *independent* structures should be considered as evidence against *C. elegans* SYG-1 dimerization through D1D2.

The models of SYG-1 D1 and D2 domains were used to molecular replace the Rst structure. This was achieved by creating homology models based on SYG-1 domains with MODELER (Eswar et al., 2006). Duf D1 structure was solved by molecular replacement using the Rst D1.

## Structure Determination of Neph1

Determination of the Neph1 D1D2 structure proved to be difficult due to the low resolution ($d_{min}$ = 3.95 Å) of the Neph1 D1D2 data set and low sequence identity between Neph1 and its orthologs. We created Rst-based homology models of Neph1, which could successfully be placed in the Neph1 data by PHASER. However, refinement with conventional methods failed, as $R$-free could not be brought down below 38%. This was circumvented with Dynamic Elastic Refinement (DEN) within CNS (Brunger, 2007; Schröder et al., 2007). The optimal DEN parameters were $\gamma = 0.7$, $\kappa = 0.1$ and $w_{den} = 100$. Following DEN, $R$-free was 34%. The model refinement was finished using tight chemical restraints with phenix.refine.

None of the molecular replacement models for SYG-1 orthologs contained the homodimers described here. Yet, they were observed in the three non-nematode SYG-1 structures. It should be noted that out of the seven crystal structures solved for SYG-1 and orthologs, the four *C. elegans* SYG-1 structures do not contain the dimeric interface commonly observed for the three non-nematode SYG-1-like structures. This constitutes an independent line of evidence for the lack of *C. elegans* SYG-1 homodimers.

## Structure Determination of SYG-2 D4

The structure of SYG-2 D4 was solved using the diffraction data obtained from a crystal derivatized with $Ta_6Br_{12}^{2+}$. The partial model that we built with phases obtained from this data set was used in molecular replacement with a native diffraction data set. The two crystals were nearly isomorphous but not enough to allow phasing with the single isomorphous replacement (SIR) method.

We processed diffraction data sets for derivatized crystals using HKL-3000 (Otwinowski and Minor, 1997; Minor et al., 2006). During the data processing, we applied computational corrections for absorption in a crystal and imprecise calculations of the Lorentz factor resulting from a minor misalignment of the goniostat (Borek et al., 2003; Otwinowski et al., 2003). We also applied the procedure to correct for the anisotropic diffraction, to adjust the error model, and to compensate the phasing signal for a radiation-induced increase of non-isomorphism within the crystal (Borek et al., 2007, 2010). All these corrections were crucial for successful phasing.

The crystals of the derivative diffracted to resolution 2.1 Å and the estimated level of anomalous signal was 10.7% of the native intensity to resolution 3.0 Å. We performed the search for heavy atom positions to resolution 2.1 Å with SHELX-D (Schneider and Sheldrick, 2002; Sheldrick, 2008), run within HKL-3000. SHELX-D found 34 positions of a heavy atom with correlations coefficients $CC_{All}$ = 36.02% and $CC_{Weak}$ = 20.16%. The handedness of the solution was determined with SHELX-E by analyzing the connectedness and contrast of electron density maps (Sheldrick, 2002). Positions of heavy atoms were refined with MLPHARE (Otwinowski, 1991) run within HKL-3000 with occupancies and temperature factors refined together. We analyzed the heavy atom positions with high temperature factors and decided to refine some of them anisotropically. This operation allowed us to identify which heavy atom positions should be split into two atoms. We expect six tantalum positions per each $Ta_6Br_{12}^{2+}$ with a 2.9 Å distance from one another. However, the $Ta_6Br_{12}^{2+}$ cluster is very symmetrical, which promotes its binding in multiple conformations, typically two overlapping ones (Banumathi et al., 2003). A moderate, 2.1 Å diffraction limit in combination with multiple conformations hinders precise determination of heavy atom positions. Therefore, we applied prior knowledge about the octahedral structure of the cluster (Knäblein et al., 1997; Neuefeind et al., 1997) to identify which of the positions with high anisotropic $B$-factors should be split into two positions. The phases obtained after the initial refinement of the heavy atom positions with MLPHARE were improved with DM (Cowtan, 1994). The peak search procedure was applied to the anomalous difference map calculated from the phases obtained with DM, and the new

peaks were refined again with MLPHARE. The iteration: DM → Peak Search → MLPHARE was repeated 20 times within HKL-3000. The end result was a fully resolved atomic structure for all conformations of the $Ta_6Br_{12}^{2+}$ cluster. Determination of the $Ta_6Br_{12}^{2+}$ clusters' atomicity was essential for successful phasing.

After the procedure, the phasing power described by the figure of merit (FOM) was 0.32. At this point, we applied density modification with PARROT (Cowtan, 2010) from the CCP4 suite (Winn et al., 2011). This was followed by model building with BUCCANEER (Cowtan, 2006), also from the CCP4 suite, which built 200 amino acids (93% of model) into the electron density, docking side chains for 104 of them (48% of the model). Then the initial model was manually cleaned of incorrectly built fragments and introduced as a starting model to another round of BUCCANEER. The final result contained 191 amino acids (88% of the model), from which 186 had been docked (86% of the model). *R*-factor and *R*-free were 42.2 and 45.8% at this point, largely because BUCCANEER did not include the diffraction from the $Ta_6Br_{12}^{2+}$ clusters. This model was used for molecular replacement with MOLREP (Vagin and Teplyakov, 1997; Lebedev et al., 2008), which is part of the CCP4 suite, against the native data set that has a diffraction limit of 1.8 Å. Alternate rounds of REFMAC (Murshudov et al., 1997) refinement with rebuilding guided by inspecting electron density maps in COOT quickly led to a complete model that was further refined with Phenix.refine.

### Structure Determination of the SYG-1/SYG-2 Complex

The structures of SYG-1 D1, SYG-1 D2, and SYG-2 D4, which we have determined using de novo phasing methods, were used as molecular replacement models with the SYG-1 D1D2/SYG-2 D1-D4 N391C data set, with the program PHASER (McCoy, 2007; McCoy et al., 2007). The asymmetric unit cell contained three copies of each molecule. Maps calculated with this ~50% complete model revealed density that could be the missing nine domains in the model (i.e., three unique domains); the *R*-free was 51% at this stage. It should be noted that at this resolution, 3.3 Å, and without experimental phases, model building of beta strands is challenging. Even the connectivity of SYG-2 domains were not clear, until we created homology models for SYG-2 D3 with MODELER (Eswar et al., 2006), which were successfully placed by PHASER in the partial model, significantly improving the overall quality of the maps (*R*-free = 49%). These maps were used to build the domain de novo manually, since the homology models were of inferior quality. Finally, we were able to manually place and build SYG-2 D1 and D2 domains, with some aid from homology models, but mostly through placing fragments of beta strands, refining the putative model with Phenix.refine, and inspecting maps and refinement statistics. After approximately forty cycles of this process, the *R*-free was down to 32%, and the domain connectivity and directions of all the strands have been confidently determined.

Also, the similarly low-resolution structure of SYG-2 D3D4 was solved with molecular replacement. This model was used to confirm the structure of SYG-2 D3 domain within the heterophilic complex model.

Finally, we do not see any evidence of significant conformational change in the SYG-1 D1 accompanying binding SYG-2; rather it appears to be a rigid, modular structural unit.

### Electron Microscopy and Image Processing

Purified SYG-1, SYG-2, and a 1:1 mixture of SYG-1 and SYG-2 cross-linked with 0.02% (v/v) (final concentration) glutaraldehyde were prepared by conventional negative staining with 0.75% (w/v) uranyl formate (Ohi et al., 2004). Images were collected with a Tecnai T12 electron microscope (FEI, Hillsboro, OR) equipped with an $LaB_6$ filament and operated at an acceleration voltage of 120 kV. Images were recorded at a nominal magnification of 42,000x and a defocus value of −1.5 μm on a 2K × 2K or a 4K × 4K charge-coupled device (CCD) camera (Gatan) using low-dose procedures. The pixel size was 2.6 Å at the specimen level.

BOXER, the display program associated with the EMAN2 software package (Tang et al., 2007), was used to interactively select particles. For SYG-1, 5763 particles were selected from 197 4K × 4K CCD images, and for SYG-2, 9433 particles were selected from 280 2K × 2K CCD images and 335 4K × 4K CCD images. The SYG-1/SYG-2 particles were selected from 174 4K × 4K CCD images. Using the SPIDER software package (Frank et al., 1996), the SYG-1 particles were windowed into 96 × 96-pixel images. The SYG-2 particles were windowed into 200 × 200-pixel images and binned by a factor of 2. The particles were rotationally and translationally aligned, and subjected to 10 cycles of multi-reference alignment. Each round of multi-reference alignment was followed by K-means classification specifying 50 output classes for SYG-1 and 100 classes for SYG-2. The references used for the first multi-reference alignment were randomly chosen from the particle images.

### *C. elegans* Transgenic Lines

Expression plasmids for transgenic worm lines were made using the pSM vector, a derivative of pPD49.26 (A. Fire). The *unc-86* promoter was cloned between SphI and XmaI and *egl-17* promoter was cloned between FseI and AscI, genes of interests were cloned between NheI and KpnI.

The following transgenic lines were used in this study:

SNB-1 marker line: *kyIs235* [*Punc-86::snb-1::yfp; Punc-4::lin-10::dsred; Podr-1::dsred*].

SYG-1 rescue expression lines: *wyEx5316/wyEx5317/wyEx5318* [*Punc-86::syg-1WT; Podr-1::gfp*], *wyEx5319/wyEx5320/wyEx5321* [*Punc-86::syg-1Q54A; Podr-1::gfp*], *wyEx5324/wyEx5325/wyEx5326* [*Punc-86::syg-1D58A; Podr-1::gfp*], *wyEx5327/wyEx5328/wyEx5329* [*Punc-86::syg-1F60A; Podr-1::gfp*], *wyEx5330/wyEx5331/wyEx5332* [*Punc-86::syg-1Q105A; Podr-1::gfp*], *wyEx5346/wyEx5347/wyEx5348* [*Punc-86::syg-1E108A; Podr-1::gfp*], *wyEx5316/wyEx5317/wyEx5318* [*Punc-86::syg-1WT; Podr-1::gfp*], *wyEx5349/wyEx5350/wyEx5351* [*Punc-86::syg-1Q54A/M56A/F60A/S107A; Podr-1::gfp*].

SYG-1 localization expression lines: *wyEx5367* [*Punc-86::syg-1WT::mCherry; Podr-1::gfp*], *wyEx5369* [*Punc-86::syg-1D58A::m-Cherry; Podr-1::gfp*], *wyEx5371* [*Punc-86::syg-1F60A::mCherry; Podr-1::gfp*], *wyEx5373* [*Punc-86::syg-1Q54A/M56A/F60A/S107A::mCherry; Podr-1::gfp*], *wyEx6303* [*Punc-86::syg-1WT::GFP; Pegl-17::syg-2; Podr-1::dsred*], *wyEx6312* [*Punc-86::CARD1-syg-1WT::mCherry; Pegl-17::JAMLD1-syg-2; Podr-1::dsred*], *wyEx6314* [*Punc-86::CD47D1-syg-1WT::mCherry; Pegl-17::SirpaD1-syg-2; Podr-1::dsred*], *wyEx6314* [*Punc-86::CD47D1-syg-1WT::mCherry; Pegl-17::SirpaFD6D1-syg-2; Podr-1::dsred*], *wyEx6320* [*Punc-86::CD47D1-syg-1WT::mCherry; Pegl-17::SirpaD1-syg-2; Podr-1::dsred*], *wyEx6322* [*Punc-86::syg-1WT::GFP; Podr-1::dsred*], *wyEx6361* [*Punc-86::syg-1-flex::GFP; Pegl-17::syg-2-flex; Podr-1::dsred*].

SYG-1 and SYG-2 rescue expression lines: *wyEx5571/wyEx5572* [*Punc-86::syg-1; Podr-1::gfp*], *wyEx5597/wyEx5598* [*Pegl-17::syg-2; Podr-1::gfp*], *wyEx5594/wyEx5595/wyEx5596* [*Punc-86:: syg-1; Pegl-17:: syg-2; Podr-1::gfp*], *wyEx5628/wyEx5629/wyEx5630* [*Punc-86::RstD1-syg-1; Pegl-17::SNSD1-syg-2; Podr-1::gfp*], *wyEx5631/wyEx5632/wyEx5633* [*Punc-86::Neph1D1-syg-1; Pegl-17::NephrinD1-syg-2; Podr-1::gfp*], *wyEx5530/wyEx5531/wyEx5532/wyEx5533* [*Punc-86::CARD1-syg-1; Pegl-17::JAMLD1-syg-2; Podr-1::gfp*], *wyEx5534/wyEx5535/wyEx5536/wyEx5537* [*Punc-86::CD47D1-syg-1; Pegl-17::SirpaD1-syg-2; Podr-1::gfp*], *wyEx5538/wyEx5539/wyEx5540/wyEx5541* [*Punc-86::CD47D1-syg-1; Pegl-17::SirpaFD6D1-syg-2; Podr-1::gfp*], *wyEx5542/wyEx5543/wyEx5544/wyEx5545* [*Punc-86::GSCD47D1-syg-1; Pegl-17::SirpaD1-syg-2; Podr-1::gfp*].

Ten-residue flexible linkers in the SYG-1-Flex and SYG-2-Flex constructs were added at domain boundaries as follows: SYG-1 D1-D2 linker, VGGGSGGGSL; SYG-1 D2-D3 linker, YGGGSGGGSR; SYG-2 D1-D2 linker, VGGGSGGGSI; SYG-2 D4-D5 linker, AGGGSGGGSI.

We note here that the crystal structures of SYG-1, SYG-2, and other Ig-CAMs have allowed us to design chimeras in such a way as to minimize linker sequences between domains and preserve rigidity. The crystal structure of the SYG-1/SYG-2 complex was also crucial for inserting flexible linkers, while not disturbing the structural domains and interaction epitopes.

## SUPPLEMENTAL REFERENCES

Afonine, P.V., Grosse-Kunstleve, R.W., Echols, N., Headd, J.J., Moriarty, N.W., Mustyakimov, M., Terwilliger, T.C., Urzhumtsev, A., Zwart, P.H., and Adams, P.D. (2012). Towards automated crystallographic structure refinement with phenix.refine. Acta Crystallogr. D Biol. Crystallogr. *68*, 352–367.

Banumathi, S., Dauter, M., and Dauter, Z. (2003). Phasing at high resolution using Ta6Br12 cluster. Acta Crystallogr. D Biol. Crystallogr. *59*, 492–498.

Borek, D., Minor, W., and Otwinowski, Z. (2003). Measurement errors and their consequences in protein crystallography. Acta Crystallogr. D Biol. Crystallogr. *59*, 2031–2038.

Borek, D., Ginell, S.L., Cymborowski, M., Minor, W., and Otwinowski, Z. (2007). The many faces of radiation-induced changes. J. Synchrotron Radiat. *14*, 24–33.

Borek, D., Cymborowski, M., Machius, M., Minor, W., and Otwinowski, Z. (2010). Diffraction data analysis in the presence of radiation damage. Acta Crystallogr. D Biol. Crystallogr. *66*, 426–436.

Bricogne, G., Vonrhein, C., Flensburg, C., Schiltz, M., and Paciorek, W. (2003). Generation, representation and flow of phase information in structure determination: recent developments in and around SHARP 2.0. Acta Crystallogr. D Biol. Crystallogr. *59*, 2023–2030.

Brunger, A.T. (2007). Version 1.2 of the Crystallography and NMR system. Nat. Protoc. *2*, 2728–2733.

Cowtan, K. (1994). "dm": An automated procedure for phase improvement by density modification. Joint CCP4 and ESF-EACBM Newsletter on Protein Crystallography *31*, 34–38.

Cowtan, K. (2006). The Buccaneer software for automated model building. 1. Tracing protein chains. Acta Crystallogr. D Biol. Crystallogr. *62*, 1002–1011.

Cowtan, K. (2010). Recent developments in classical density modification. Acta Crystallogr. D Biol. Crystallogr. *66*, 470–478.

Doublié, S. (2007). Production of selenomethionyl proteins in prokaryotic and eukaryotic expression systems. Methods Mol. Biol. *363*, 91–108.

Garboczi, D.N., Hung, D.T., and Wiley, D.C. (1992). HLA-A2-peptide complexes: refolding and crystallization of molecules expressed in Escherichia coli and complexed with single antigenic peptides. Proc. Natl. Acad. Sci. USA *89*, 3429–3433.

Garboczi, D.N., Utz, U., Ghosh, P., Seth, A., Kim, J., VanTienhoven, E.A., Biddison, W.E., and Wiley, D.C. (1996). Assembly, specific binding, and crystallization of a human TCR-alphabeta with an antigenic Tax peptide from human T lymphotropic virus type 1 and the class I MHC molecule HLA-A2. J. Immunol. *157*, 5403–5410.

Kabsch, W. (2010). XDS. Acta Crystallogr. D Biol. Crystallogr. *66*, 125–132.

Knäblein, J., Neufeind, T., Schneider, F., Bergner, A., Messerschmidt, A., Löwe, J., Steipe, B., and Huber, R. (1997). Ta6Br(2+)12, a tool for phase determination of large biological assemblies by X-ray crystallography. J. Mol. Biol. *270*, 1–7.

Lebedev, A.A., Vagin, A.A., and Murshudov, G.N. (2008). Model preparation in MOLREP and examples of model improvement using X-ray data. Acta Crystallogr. D Biol. Crystallogr. *64*, 33–39.

McCoy, A.J. (2007). Solving structures of protein complexes by molecular replacement with Phaser. Acta Crystallogr. D Biol. Crystallogr. *63*, 32–41.

McCoy, A.J., Grosse-Kunstleve, R.W., Adams, P.D., Winn, M.D., Storoni, L.C., and Read, R.J. (2007). Phaser crystallographic software. J. Appl. Cryst. *40*, 658–674.

Minor, W., Cymborowski, M., Otwinowski, Z., and Chruszcz, M. (2006). HKL-3000: the integration of data reduction and structure solution—from diffraction images to an initial model in minutes. Acta Crystallogr. D Biol. Crystallogr. *62*, 859–866.

Murshudov, G.N., Vagin, A.A., and Dodson, E.J. (1997). Refinement of macromolecular structures by the maximum-likelihood method. Acta Crystallogr. D Biol. Crystallogr. *53*, 240–255.

Neufeind, T., Bergner, A., Schneider, F., Messerschmidt, A., and Knablein, J. (1997). The suitability of Ta6Br12(2+) for phasing in protein crystallography. Biol. Chem. *378*, 219–221.

Otwinowski, Z. (1991). Maximum likelihood refinement of heavy atom parameters. CCP4 Study Weekend, 80–86.

Otwinowski, Z., and Minor, W. (1997). Processing of X-ray diffraction data collected in oscillation mode. In Methods in Enzymology, *Volume 276* (New York: Academic Press), pp. 307–326.

Otwinowski, Z., Borek, D., Majewski, W., and Minor, W. (2003). Multiparametric scaling of diffraction intensities. Acta Crystallogr. A *59*, 228–234.

Schneider, T.R., and Sheldrick, G.M. (2002). Substructure solution with SHELXD. Acta Crystallogr. D Biol. Crystallogr. *58*, 1772–1779.

Sheffield, P., Garrard, S., and Derewenda, Z. (1999). Overcoming expression and purification problems of RhoGDI using a family of "parallel" expression vectors. Protein Expr. Purif. *15*, 34–39.

Sheldrick, G.M. (2002). Macromolecular phasing with SHELXE. Z. Kristallogr. *217*, 644–650.

Sheldrick, G.M. (2008). A short history of SHELX. Acta Crystallogr. A *64*, 112–122.

Sheldrick, G.M. (2010). Experimental phasing with SHELXC/D/E: combining chain tracing with density modification. Acta Crystallogr. D Biol. Crystallogr. *66*, 479–485.

Vagin, A., and Teplyakov, A. (1997). MOLREP: an Automated Program for Molecular Replacement. J. Appl. Cryst. *30*, 1022–1025.

Vonrhein, C., Blanc, E., Roversi, P., and Bricogne, G. (2007). Automated structure solution with autoSHARP. Methods Mol. Biol. *364*, 215–230.

Winn, M.D., Ballard, C.C., Cowtan, K.D., Dodson, E.J., Emsley, P., Evans, P.R., Keegan, R.M., Krissinel, E.B., Leslie, A.G.W., McCoy, A., et al. (2011). Overview of the CCP4 suite and current developments. Acta Crystallogr. D Biol. Crystallogr. *67*, 235–242.
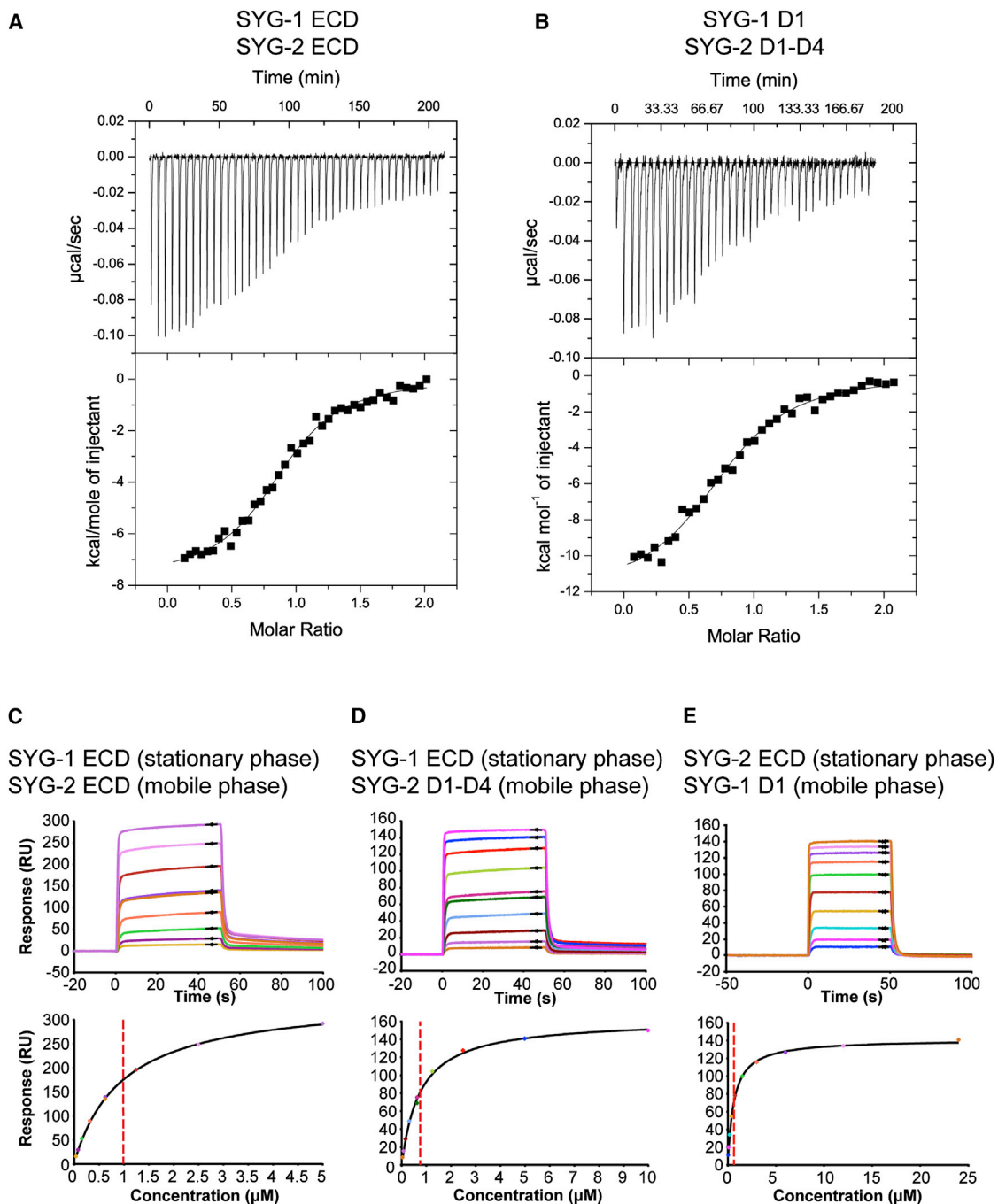
**Figure S1. ITC Titration Results and SPR Sensorgrams for *C. elegans* SYG-1 and SYG-2 and Their Domain Truncations, Related to Figure 1**
(A and B) ITC titrations and data fitting for full ectodomains of SYG-1 and SYG-2 (A), and SYG-1 D1 and SYG-2 D1-D4.
(C–E) SPR sensorgrams and equilibrium response fitting to a Langmuir model for SYG-1 ECD with SYG-2 ECD (C), SYG-1 ECD with SYG-2 D1-D4 (D), and SYG-2 ECD with SYG-1 D1 (E). See Table S1 for a summary of determined affinity parameters.
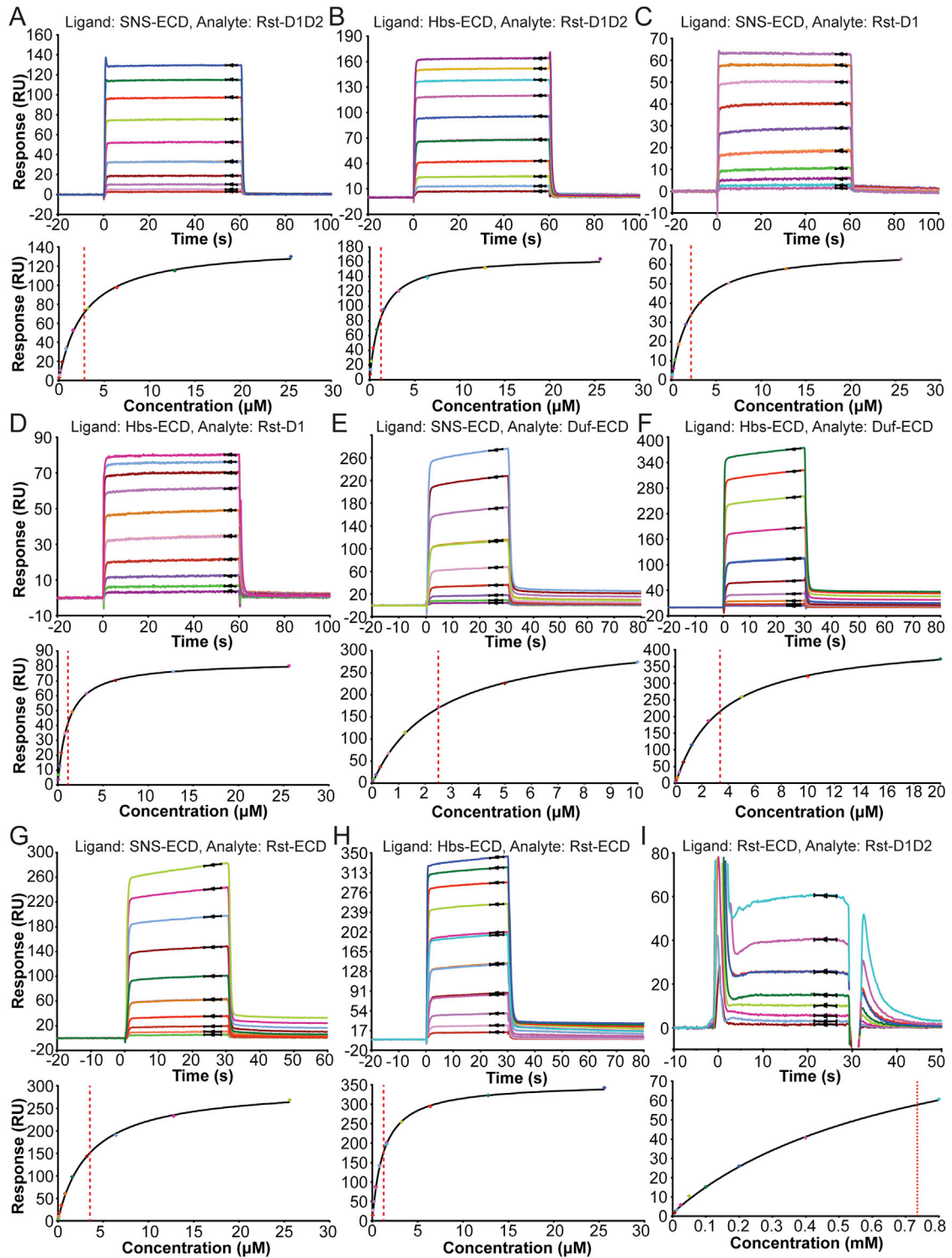
**Figure S2. Surface Plasmon Resonance Sensorgrams for *Drosophila* SYGs and Their Domain Truncations, Related to Figure 2**
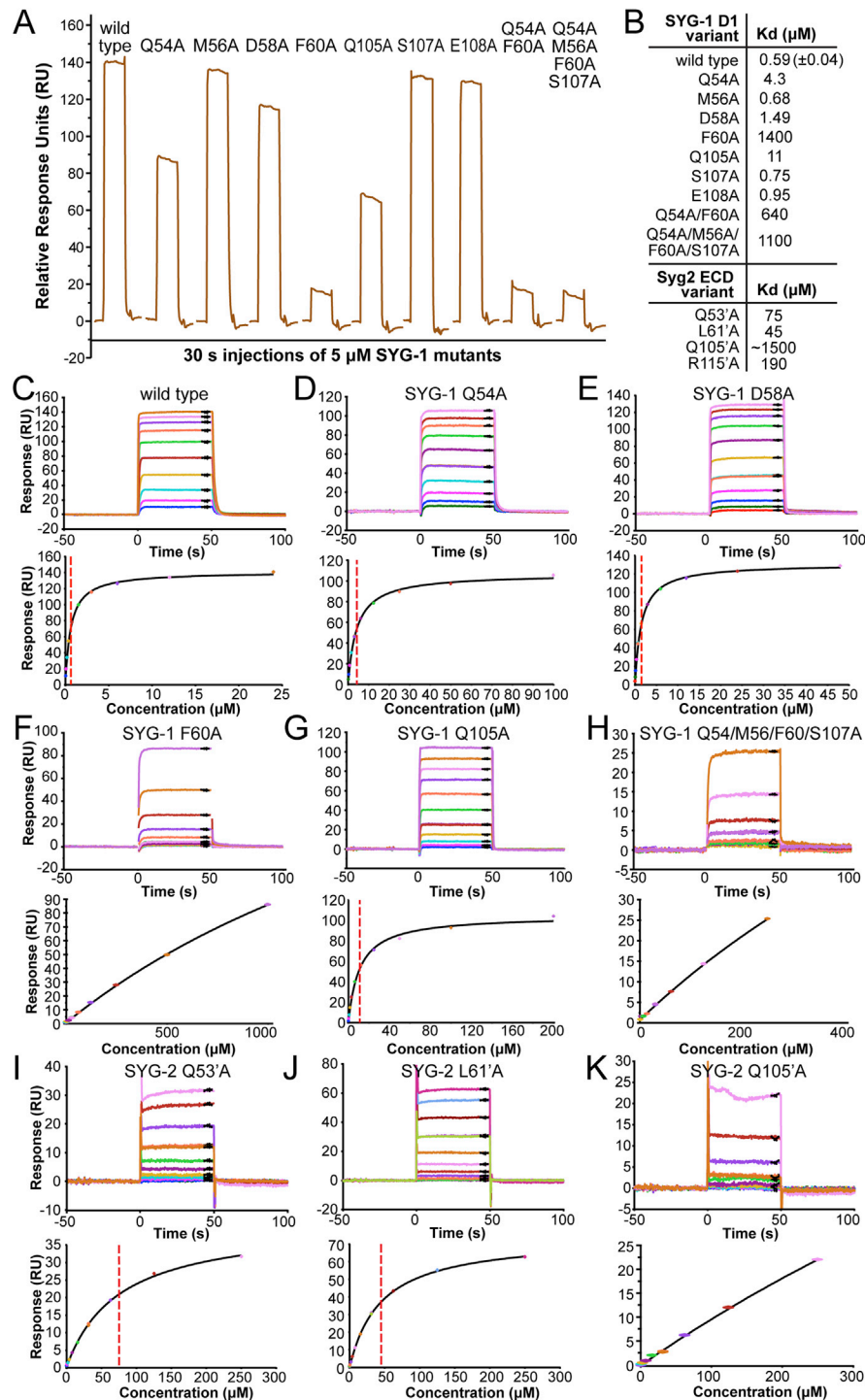(A–I) See Table S1 for a summary of determined affinity parameters.

**Figure S3. Surface Plasmon Resonance Sensorgrams for the Interaction of *C. elegans* SYG-1 D1 and Its Mutants with Full Ectodomain of SYG-2, Related to Figure 3**

(A) SPR sensorgrams for short, sequential injections of all SYG-1 D1 mutants on a SYG-2-captured surface. SYG-1 D1 variants are at 5 μM. This approximately results in 89% saturation of SYG-2 surface for wild-type protein, based on the Langmuir model and a $K_d$ value of 0.59 μM. $K_d$ values for all mutants can be estimated from responses to these standardized injections.

(B) Tabulated affinities ($K_d$) for all SYG-1 D1 variants to the SYG-2 ectodomain, and SYG-2 ectodomain variants to wild-type SYG-1 D1. These values were calculated by full titration series equilibrium binding experiments with SPR, as seen in (C) to (K), and agree fully with the analysis done in (A).

(C–K) SPR sensorgrams for six SYG-1 D1 variants binding to SYG-2 ECD (C-H), and three SYG-2 ectodomain variants binding to SYG-1 D1 (I-K).
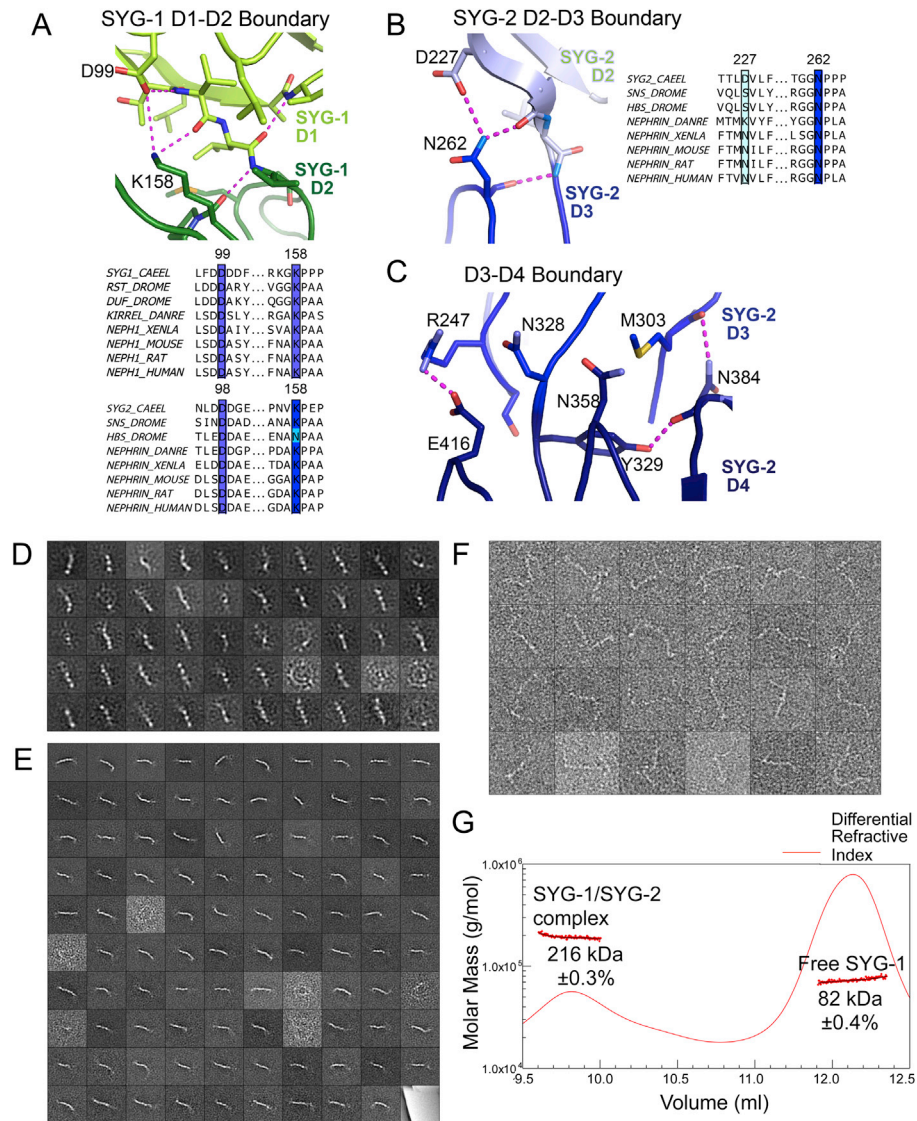
**Figure S4. Structural Conformations and Stoichiometry of the Full Ectodomains of SYG-1, SYG-2, and Their Complex, Assessed by Electron Microscopy, Multiangle Light Scattering, and Crystallography, Related to Figure 4**

(A) SYG-1 D1-D2 boundary. A close-up view of the SYG-1 D1-D2 boundary from our refolded SYG-1 D1D2 crystal structure, showing close packing of D1 (light green) and D2 (dark green), and polar interactions between them (salt bridges and hydrogen bonds) labeled as dashes. The sequence alignment below demonstrates that residues involved in these polar interactions are nearly universally conserved in all SYG-1 and SYG-2 orthologs. The residue numbers on the SYG-1 and SYG-2 alignments are for *C. elegans* orthologs.

(B) SYG-2 D2-D3 boundary. A close-up of the SYG-2 D2-D3 boundary from our SYG-1 D1D2/SYG-2 D1-D4 N391C crystal structure, showing the interactions mediated by N262 at the domain interface (D2 is in light blue, and D3 is in blue). The alignment to the right shows that N262 is universally conserved in SYG-2 orthologs.

(C) SYG-2 D3-D4 boundary. A close-up of the SYG-2 D3-D4 boundary, showing the thorough packing between the two domains, where polar interactions are labeled as dashes. D4 is colored as dark blue.

(D) Averages of EM images of SYG-1 ECD in negative stain obtained by classifying 5,763 particles into 50 classes. The side length of the individual panels is 25 nm.

(E) Averages of EM images of SYG-2 ECD in negative stain obtained by classifying 9,433 particles into 100 classes. The side length of the individual panels is 50 nm.

(F) Gallery of cross-linked SYG-1/SYG-2 complexes in negative stain. The side length of the individual panels is 50 nm. The complexes show a 1:1 complex, which is consistent with our ITC (Figure S1) and multi-angle light scattering (Figure S4G) data.

(G) Multi-angle (static) light scattering of the SYG-1 ECD/SYG-2 ECD complex eluting from a size exclusion column (Shodex KW-803) with excess free SYG-1. The SYG-1/SYG-2 complex is 1:1 in solution. See *Extended Experimental Protocols* for details.
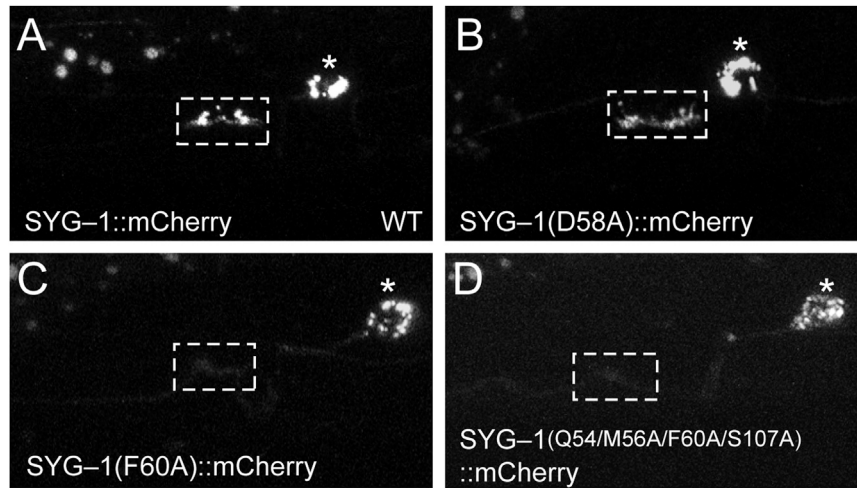
**Figure S5. SYG-1-SYG-2 Interaction Leads to SYG-1 Clustering at the Vulva, Related to Figure 5**

(A) Fluorescence images of SYG-1::mCherry as SYG-1 is clustered at the vulva, where it binds SYG-2.

(B) SYG-1 D58A has partial affinity to SYG-2, and still gets clustered at the vulva.

(C and D) SYG-1 mutants F60A and the quadruple mutant have negligible affinity for SYG-2, and therefore do not accumulate at the vulva.
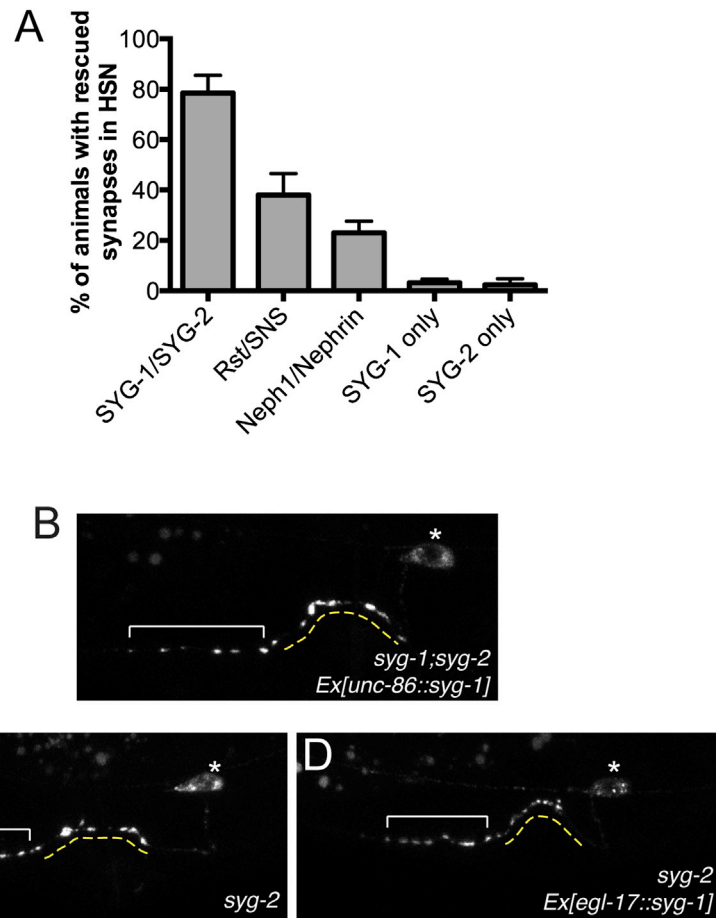
**Figure S6. SYG-1 ECD Cannot Substitute for SYG-2 ECD Functionally, Related to Figure 6**

(A) Quantitation of rescue (as phenotype scores) of *syg-1;syg-2* worms when D1s are replaced by D1 domains from indicated proteins. Controls are SYG-1 only and SYG-2 only, in which cases only *syg-1* and only *syg-2* are injected to *syg-1;syg-2* animals.

(B) Injection of *Punc86::syg-1* alone fails to rescue the synapses in the *syg-1;syg-2* mutant.

(C) *syg-2* mutant worms show ectopic accumulations of synaptic vesicles in the anterior axon of the HSNL neuron.

(D) *syg-2* mutant worms injected with *Pegl-17::syg-1* does not rescue the synapse defects in HSNL. This indicates that a SYG-1/SYG-1 *trans* homodimer does not form, or if it did, it does not rescue synaptic defects of *syg-2* mutants.